Three-Dimensional Model Simulations of Tides and Buoyancy Currents along the West Coast of Vancouver Island

MICHAEL G. G. FOREMAN AND RICHARD E. THOMSON

Department of Fisheries and Oceans, Institute of Ocean Sciences, Sidney, British Columbia, Canada

(Manuscript received 25 June 1996, in final form 3 December 1996)

ABSTRACT

A three-dimensional finite element model is used to calculate the barotropic tides and seasonal buoyancy flows off the western and northern coasts of Vancouver Island. The model buoyancy currents and the harmonics of eight tidal constituents are compared with those from previous models, and those from tide gauge and current meter observations. The rms differences between observed and calculated sea level tidal amplitudes are within 2.3 cm for all constituents, whereas the rms differences between observed and calculated phases are, with the exception of Q_1, within 3.5°. The model currents are more accurate than those from previous models.

Of particular interest are the diurnal continental shelf waves. It is shown that these waves are generated through the conservation of potental vorticity arising when the strong diurnal tidal currents in Juan de Fuca Strait encounter the abrupt topography near the entrance to the strait. These waves do not appear to propagate beyond Brooks Peninsula, a large promontory cutting across the continental shelf. A power budget analysis reveals that the reason for this is not the blocking effect of the peninsula but rather there is little energy left in the waves when they reach that point. This energy loss is primarily through frictional dissipation in a series of trapped eddies along the shelf break. The location of these eddies varies with the forcing frequency and appears to be related to the spacing of canyons. It is also demonstrated that the strong diurnal currents observed over the shallow banks in Queen Charlotte Sound to the north of Brooks Peninsula do not arise from the oscillatory diurnal flows in Queen Charlotte Strait. Unlike the case for Juan de Fuca Strait, the region offshore of Queen Charlotte Strait does not support diurnal coastally trapped waves. Seasonal changes in the wavelengths of the Vancouver Island shelf waves are shown to arise through an advective interaction (Doppler shift) with the buoyancy-driven Vancouver Island coastal current and the wind-driven shelf break current.

1. Introduction

This paper describes the development and evaluation of a three-dimensional model for calculating seasonal buoyancy flows and barotropic tides in western Juan de Fuca Strait, northwestern Washington State, and the continental shelf and slope off the western and northern coasts of Vancouver Island (Fig. 1). Flather (1988, henceforth F88) simulated the M_2 and K_1 constituents in a subset of this region with a two-dimensional (2D) finite difference model, while Foreman and Walters (1990, henceforth FW90) used a 2D finite element technique to simulate eight constituents for the southern portion of the shelf. Although F88 demonstrated that almost all of the shelf wave component in constituent K_1 arises from oscillatory flows in Juan de Fuca Strait, his calculated current speeds were generally too large and his wavelengths were too short. The summer buoyancy-driven flows have also been previously calculated in a subset of this region by Foreman et al. (1992), but no attempt was made to quantatively evaluate their accuracy.

Except in the vicinity of Brooks Peninsula, the western margin of Vancouver Island is characterized by an extensive shelf, steep slope, and broad continental rise (Fig. 2). As delineated by the 200-m depth contour, the continental shelf attains a maximum width in excess of 65 km westward of Juan de Fuca Strait and narrows northward to about 5 km off Brooks Peninsula. In Queen Charlotte Sound, off the northern end of Vancouver Island, the shelf widens to as much as 150 km before narrowing northward into the semienclosed Hecate Strait. Off southern Vancouver Island, the shelf has a particularly convoluted geometry consisting of numerous shallow banks (e.g., Swiftsure, Amphitrite, La Pérouse) separated by a series of deep basins roughly 100 m and the Juan de Fuca Canyon, which is approximately 10 km wide and over 300 m deep in some regions. Lesser canyons such as Nitinat, Barkley, Clayquot, and Nootka lie north of Juan de Fuca and although they do not bisect the shelf, it will be seen that they do affect the diurnal shelf waves. Westward of Washington State, the depth contours are more uniform and are roughly parallel to the coast. Queen Charlotte Sound is char-

Corresponding author address: Dr. Michael G. G. Foreman, Institute of Ocean Sciences, P.O. Box 6000, W. Saanich Rd., Sidney, BC V8L 4B2, Canada.
E-mail: mforeman@mike.ios.bc.ca

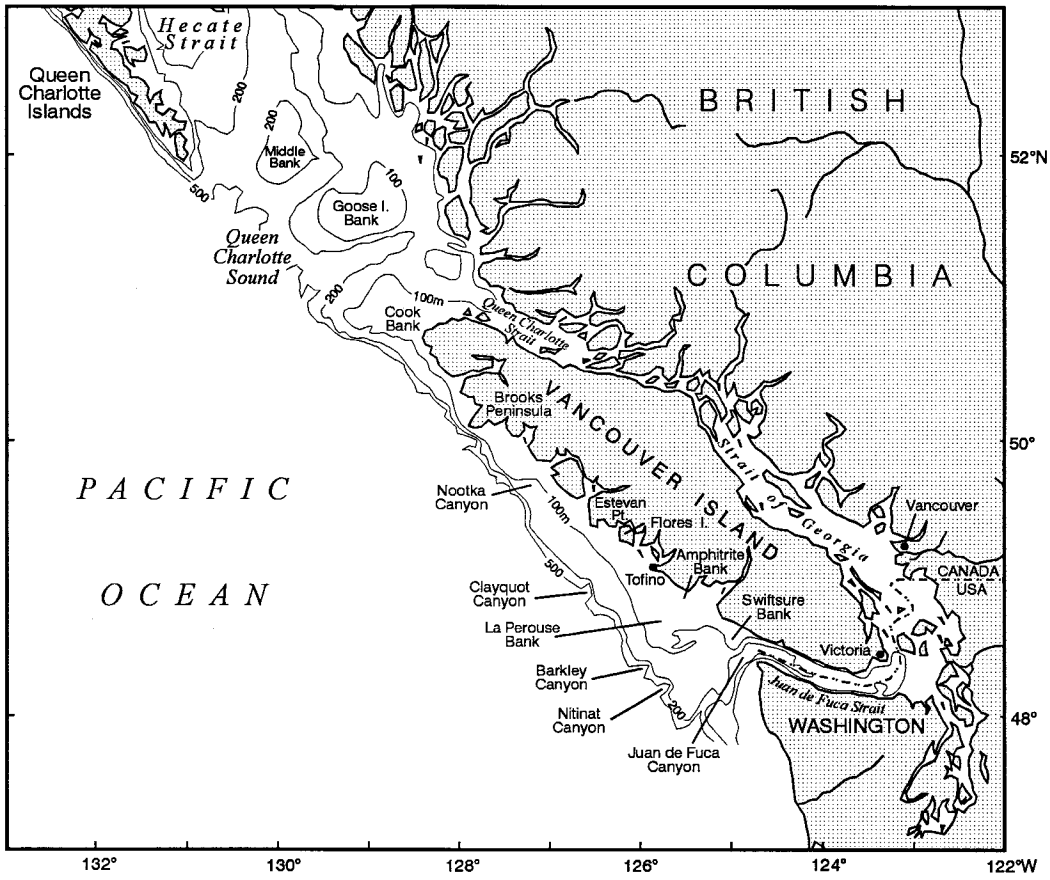

FIG. 1. Geography and depth contours (m) for the south coast of British Columbia and the north coast of Washington State. The international boundary is denoted with a dash–dot line.

acterized by three relatively deep troughs that separate Cape St. James, Middle Bank, Goose Island Bank, and Cook Bank.

Flows off northern and western Vancouver Island consist of tidal currents, wind-generated currents, the buoyancy-driven Vancouver Island coastal current, and a seasonal shelf break current. Freeland et al. (1984) and Thomson et al. (1989) have described the origins and nature of these last two currents. The tides have been extensively measured and their general characteristics are discussed in Flather (1987, 1988) and FW90. Thomson (1981) provides further descriptions of the physical oceanography of the region.

Using current meter observations from three lines of cross-shelf moorings and a mode decomposition based on Brink's (1982) analytic shelf wave model, Crawford and Thomson (1984) showed that 95% of the K_1 current variance off southern Vancouver Island can be explained by a barotropic Kelvin wave and a first mode baroclinic shelf wave. Despite that the shelf wave accounts for 99% of these two components, F88 demonstrated that a barotropic model can reproduce the wave with reasonable accuracy. As noted by Crawford (1984), this is because over the continental shelf the diurnal-period current ellipses are basically uniform with depth. Only when currents over the slope are examined do any baroclinic effects emerge.

Crawford and Thomson (1984) also showed that the O_1 shelf wave wavelength is longer than the K_1 wavelength and both wavelengths become longer in winter. It was speculated that this shift was due to an interaction with the seasonally varying, wind-driven, shelf-break current, rather than seasonal changes in stratification. Flather (1988) qualitatively confirmed this hypothesis by demonstrating that the wavelength of his K_1 shelf wave became longer in the presence of currents forced by a 0.23 N m^{-2} wind stress from the southeast. Since these studies, several more current meter time series have been collected as part of the Coastal Current Experiment (Thomson et al. 1989; Hickey et al. 1991) and the La Pérouse Project (Ware and Thomson 1993). Analyses of these records will be used here as they permit a better definition of the shelf wave and a more extensive verification of the numerical model.

The primary objective of this study was to improve the accuracy and realism of previous two-dimensional models so that larvae drift simulations similar to those described by Werner et al. (1993) could be conducted

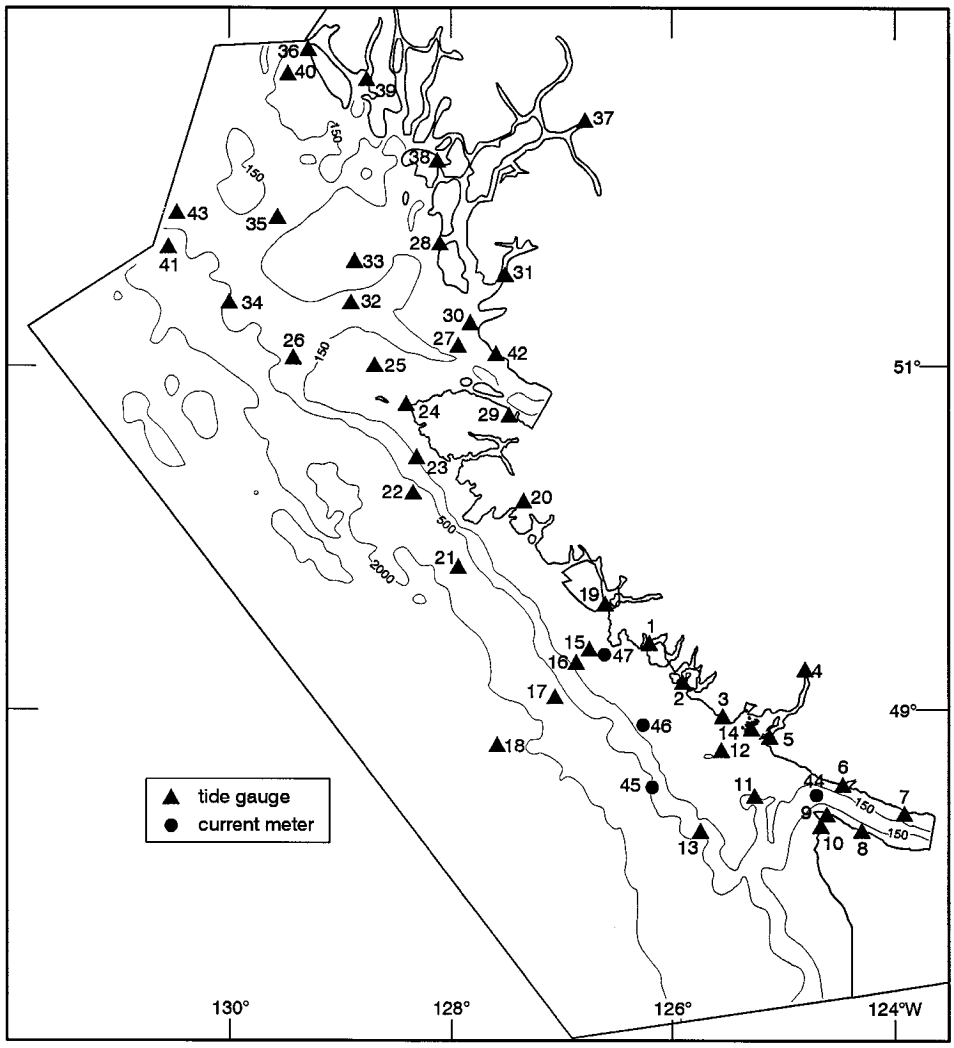

FIG. 2. Tide gauge and current meter observation sites for evaluating the performance of the tidal model. The numbered tide gauge sites are listed in Table 1. The numbered current meter sites are J2 (44), A1 (45), T4 (46), and E01 (47). Depth contours are in meters.

in this region. This improvement was attained with a much finer horizontal resolution and by extending the models to three dimensions. A secondary objective was to extend the model region northward into Queen Charlotte Sound in order to determine if the large diurnal currents observed around Goose Island, Cook, and Middle Banks (Foreman et al. 1993) are linked to the Vancouver Island shelf waves or arise in an analogous manner to those seaward of Juan de Fuca Strait via the oscillatory flows in Queen Charlotte Strait (see Figs. 1 and 2). In particular, we wished to determine if the shelf waves generated in Juan de Fuca Strait extend beyond Brooks Peninsula, a fact not apparent from the results of Flather's model. An analytical model presented by Wilmott and Thomson (1994) suggests that there is negligible diurnal shelf wave generation in Queen Charlotte Strait.

Although the study presented here is specific to the waters off Vancouver Island, certain aspects of the analysis and results should be relevant to other regions of the world with diurnal continental shelf waves (e.g., Xing and Davies 1996; Kowalik and Proshutinsky 1993; Rabinovich and Zhukov 1984). However, it should be stressed that a major limitation of the present study is that the three-dimensional (3D) density field is fixed in time. In particular, this means that baroclinic shelf waves and internal tides cannot be represented. [Internal tides have been studied along the Vancouver Island shelf by Drakopoulos and Marsden (1992) and have recently been modeled along the north coast of British Columbia by Cummins and Oey (1997).] It also means that secondary effects of the internal tides are not included in the model. As pointed out by one of the reviewers, seasonal changes in stratification will affect the intensity of the internal tides and could give rise to enhanced bottom currents and frictional dissipation, which will in

turn affect the propagation of both diurnal and semidiurnal barotropic tides.

Incorporation of these baroclinic features into both a prognostic and a diagnostic model is presently being investigated and will be reported in a future manuscript. Nevertheless, it will be demonstrated that the present 3D barotropic model permits a reasonably accurate representation of the shelf waves and an evaluation of the seasonal interaction of tidal and nontidal flows through the advection and bottom friction terms in the momentum equations.

This paper is organized as follows. In section 2, the numerical technique and the triangular grid are briefly described. In section 3, tidal heights and currents are presented for eight astronomical constituents. These are compared with previous model results and extensive tide gauge and current meter observations. In sections 4 and 5, experiments and analyses reveal the generation mechanisms and seasonality of the shelf waves. In sections 6 and 7, energy flux, power, and resonance calculations are performed, and finally, in section 8, the results are summarized and future work is outlined.

2. The numerical technique

The numerical technique used to calculate the three-dimensional tides and buoyancy currents is virtually the same harmonic, wave equation method used in Walters (1992), Foreman et al. (1995), and Ballantyne et al. (1996). Aside from the nonlinear expansions, it is also similar to the methods employed by Lynch et al. (1992), Lynch and Naimie (1993), and Naimie et al. (1994). In particular, the model solves the three-dimensional, shallow-water equations with conventional hydrostatic and Boussinesq assumptions, and viscosity closure in the vertical. The governing equations are the continuity equation

$$\nabla\cdot\mathbf{u} + \frac{\partial w}{\partial z} = 0, \tag{1}$$

its two-dimensional vertical average

$$\frac{\partial \eta}{\partial t} + \nabla\cdot(H + \eta)\bar{\mathbf{u}} = 0, \tag{2}$$

and the horizontal components of the three-dimensional momentum equation

$$\frac{\partial \mathbf{u}}{\partial t} + \nabla\cdot(\mathbf{uu}) + \mathbf{f}\times\mathbf{u} + g\nabla\eta - \frac{\partial}{\partial z}\left(A_z\frac{\partial \mathbf{u}}{\partial z}\right) = \mathbf{b}, \tag{3}$$

with surface and bottom boundary conditions

$$A_z\frac{\partial \mathbf{u}}{\partial z} = H\psi \qquad (z = 0) \tag{4}$$

and

$$A_z\frac{\partial \mathbf{u}}{\partial z} = k|\mathbf{u}|\mathbf{u} \qquad (z = -H). \tag{5}$$

The variables are defined as

(x, y, z)	eastward, northward, and upward spatial coordinates
t	time
$\eta(x, y, t)$	surface elevation relative to mean water level
$\mathbf{u}(x, y, z, t)$	horizontal velocity
$w(x, y, z, t)$	vertical velocity
$\bar{\mathbf{u}}(x, y, t)$	vertical average of $\mathbf{u}$
$H(x, y)$	depth from the mean water level
$\mathbf{f}$	Coriolis vector
g	gravity
k	bottom stress coefficient
$A_z(x, y, z, t)$	vertical viscosity parameter
∇	horizontal gradient operator $(\partial/\partial x, \partial/\partial y)$
$H\psi(x, y)$	wind stress forcing
$\mathbf{b}(x, y, z, t)$	baroclinic forcing.

As in Ballantyne et al. (1996), the baroclinic forcing is defined as

$$\mathbf{b}(x, y, z, t) = 0 \tag{6}$$

for the barotropic tides, and

$$\mathbf{b}(x, y, z) = -\frac{g}{\rho_0}\int_z^0 \nabla\rho\, dz \tag{7}$$

for the buoyancy-driven flows; $\rho(x, y, z)$ is the fluid density. Similar to Walters (1996) and Foreman et al. (1995), the vertical viscosity is defined as

$$A_z(x, y, z, t) = A_0\kappa|\mathbf{u_b}|\left(0.9\frac{z + H}{0.2H} + 0.1\right)H_e \qquad -H + z_0 \le z \le -0.8H \tag{8}$$

$$A_z(x, y, z, t) = A_0\kappa|\mathbf{u_b}|H_e \qquad z \ge -0.8H, \tag{9}$$

where $\mathbf{u_b}(x, y, t)$ is the bottom velocity, $\kappa = 0.4$ is von Kármán's constant, $z_0 = 1$ m is the height above the sea bed at which the quadratic bottom friction is deemed to be valid (Aldridge and Davies 1993), and H_e is an Ekman layer depth, assumed to be the shallower of H and 50 m. Runs were also made with the Ekman layer specified as $H_e = 0.4u_*/f$ (Davies 1990), where u_* is the bed friction velocity. As the results were found to differ ony slightly from those reported in the next section we conclude that the particular specification for H_e is not critical.

Although the governing equations are not expressed in spherical coordinates, the grid units are measured with respect to a Universal Transverse Mercator (UTM) projection (McDonnell 1979). This projection is widely used for mapping and military purposes. Even though the longitudinal range of the model domain (from approximately 124° to 132°E) is slightly larger than the 6° width of standard UTM zones, choosing the central meridian to be 127° produces only a small range of

0.9996 to 1.001 in the scaling factor. Thus, grid distances and element areas are very close to their true values.

For all subsequent model results, the Coriolis parameter assumed its true variation with latitude, $k = 0.01$, and $A_0 = 0.1$ m^2 s^{-1}. These latter two values were determined on the basis of sensitivity studies that compared model currents against observations from moorings with instruments at a minimum of two depths. Although the bottom friction coefficient may vary spatially (e.g., Gross and Werner 1994), such variations were not investigated here. Similarly, the tide generating potential, the earth tide, and ocean loading were not included in the simulations since their effects have been shown to be minor for a model domain of approximately the same size (Foreman et al. 1993).

Numerous studies also suggest that the vertical viscosity coefficient should reflect stratification (e.g., Loder and Wright 1985). To investigate the effects of such a dependency, several tests were performed where A_z varied with the Richardson number in a manner similar to that suggested by Munk and Anderson (1948) and used by Naimie et al. (1994). In general, the tidal and buoyancy currents were found to be both larger than those calculated without the stratification dependency and less accurate when compared to current meter observations. Although the reasons underlying this behavior warrant further investigation, this has been left for future studies with a prognostic baroclinic model. A stratification dependency in A_z was therefore not used in the calculation of any of the following results.

The numerical technique assumes an $e^{i\omega t}$ time dependency for each tidal constituent with frequency ω and the coupling between different frequencies that arises from the nonlinear interactions is handled by an iterative solution of the numerical equations. The technique is an extension of the approach developed by Snyder et al. (1979), for the two-dimensional shallow water equations in a finite difference context, to three dimensions and the wave equation finite element method. Steady-state buoyancy and tidal residual solutions are assumed to have zero frequency. It should be noted that the numerical results are sufficiently robust that that no explicit horizontal viscous term is required for smoothing. This is because there is some inherent filtering due to the nodal quadrature scheme that is used for the Galerkin integrations, and an element-based averaging that is employed to evaluate the advective terms.

Although only eight tidal constituents (M_2, S_2, N_2, K_2, K_1, O_1, P_1, and Q_1) are included in the boundary forcing, the presence of nonlinear terms in the governing equations means that a residual tide and several compound tides and overtides will be generated within the model domain. Only the original eight forcing constituents are discussed here. They comprise approximately 85% of the observed tidal height range and 83% of the observed tidal current speeds near Tofino.

Boundary conditions for the tidal model are zero flow normal to the coast, specified elevations or specified directions along the open sea, and specified depth-averaged velocities in Juan de Fuca and Queen Charlotte straits. The elevation amplitudes and phases for the southern and western boundaries were taken from a combination of harmonics calculated from offshore pressure time series and an update of the world tidal model of Egbert et al. (1994) that assimilates 76 cycles (approximately 760 days) of altimeter measurements from the TOPEX/POSEIDON satellite. The Juan de Fuca Strait velocities were obtained from Foreman et al. (1995), while the northern boundary elevations and the Queen Charlotte Strait velocities were obtained from Foreman et al. (1993). The buoyancy-driven currents used in this simulation were calculated similarly to the diagnostic calculations described in Ballantyne et al. (1996), Foreman et al. (1992), and Naimie et al. (1994).

The triangular grid for the finite element model (Fig. 3) was created using the Henry and Walters (1993) package of interactive computer programs. In general, this grid is a compromise among the following design requirements: (i) close fitting of the coastline, (ii) near-equilateral element shape, and (iii) an element size that decreases with strong gradients in the velocity, elevation, and bathymetric fields, yet does not have sufficiently rapid transitions to cause energy trapping (Vichnevetsky 1987). In order to represent the shelf waves more accurately, higher resolution was placed along the shelf slope in accordance with the studies of Hannah and Wright (1995), Luettich and Westerink (1995), and Heaps et al. (1988). The grid has 13 797 nodes, 25 816 triangles, and triangle sides that vary from approximately 12 km offshore to less than 1 km over some of the banks, near the coast, and along the continental slope. The northwest boundary was chosen to lie along the trench between Middle Bank and the Queen Charlotte Islands in order to avoid the stong flows located off the southern tip of those islands (Ballantyne et al. 1996) and to avoid crossing any closed f/h contours.

Tests were performed with both 11 and 21, equally spaced, sigma-coordinate layers in the vertical discretization. Differences in the two solutions were small so the subsequent presentation is restricted to results obtained with 11 layers. The potential numerical problems (Haney 1991) arising with this coordinate system when horizontal density gradients are calculated near rapid changes in bathymetry are avoided here by evaluating the baroclinic forcing initially along level surfaces before their interpolation to the sigma surfaces. Fortunato and Baptista (1996) have shown that the transformation from sigma-surface gradients to horizontal gradients, as required for the advective terms in the momentum equations, does not seem to cause analogous problems to those described by Haney (1991).

3. Tidal model evaluations

Tidal model elevations and currents were evaluated through comparisons with observations at the 43 tide

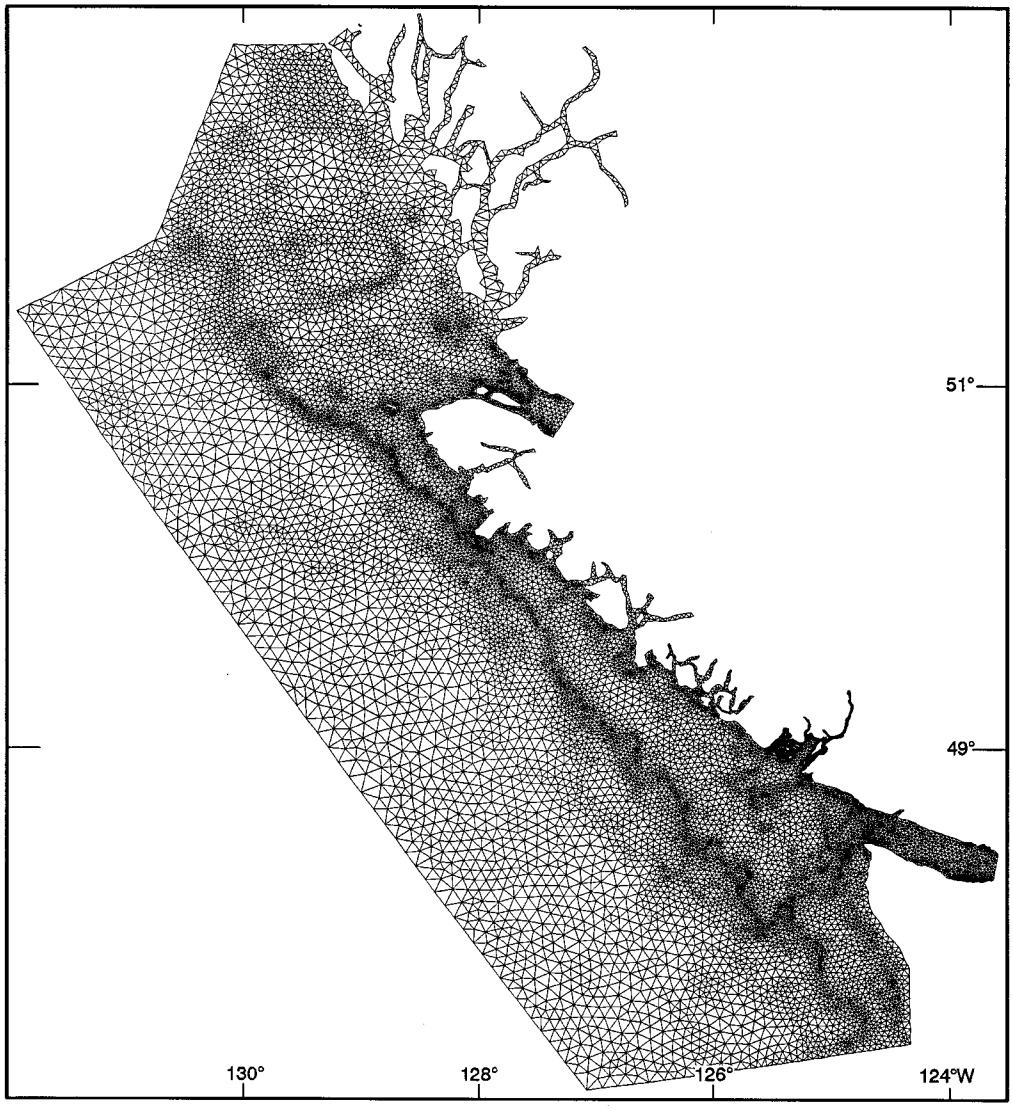

FIG. 3. Triangular grid for the finite element model.

gauge sites and the four current meter mooring locations shown in Fig. 2. This set augments those longer than 60 days in FW90 with similar time series from locations farther northward.

Table 1 shows observed and calculated M_2 and K_1 elevation amplitudes and phases for the tidal stations. All model values were determined by interpolating from the nodal values to the exact observation location. Differences between the two sets of harmonic constants are calculated as distances in the complex plane; that is,

$$D = \{(A_o\cos g_o - A_m\cos g_m)^2 + (A_o\sin g_o - A_m\sin g_m)^2\}^{1/2}, \quad (10)$$

where A_o, g_o, and A_m, g_m are the observed and modeled amplitudes and phases. The largest M_2 differences occur at Bella Coola (site 37 in Fig. 2), QC13 (41), and Milne Island (39), sites that were also problematic in Foreman et al. (1993). Bella Coola is difficult because it is at the end of a fiord where the model resolution is inadequate and the true dissipation (via bottom and sidewall friction and the generation of internal tides over sills) has not been represented accurately by the model. (However, it is interesting to note that Port Alberni, also at the end of a fiord, is reasonably accurate.) The inaccuracies at QC13 and Milne Island are puzzling in light of the much better agreement between model and observation at nearby stations such as Q06 (43). Some adjustments to the northern boundary condition could probably improve the discrepancies, but this was not done. The largest K_1 difference occurs at Kyuquot (20), another site at the head of an inlet.

Table 2a shows root-mean-square (rms) sea level amplitude and phase values for each of the eight major

TABLE 1. Observed and calculated M_2 and K_1 elevation amplitudes (cm) and phases (deg, UTC) for the numbered sites shown in Fig. 2. D (cm), a measure of their difference, is calculated with Eq. (8). Those sites denoted * were also used to validate the Flather (1988) model.

				M_2				
				Observed		Model		
Site	Site	Lat	Long	Amp	Phase	Amp	Phase	D
1	Riley Cove*	49.383	126.217	98.8	239.2	98.4	239.5	0.7
2	Tofino*	49.154	125.912	99.1	240.7	97.7	238.5	4.1
3	Ucluelet*	49.950	125.550	93.4	235.8	93.5	235.7	0.2
4	Port Alberni	49.229	124.812	96.0	235.7	95.9	235.1	1.0
5	Bamfield*	48.833	125.133	93.8	235.2	93.1	234.7	1.1
6	Port San Juan*	48.545	124.480	69.9	241.0	72.2	241.2	2.3
7	Sheringham Point*	48.375	123.918	48.7	263.3	49.8	260.1	3.0
8	Sekiu*	48.267	124.300	66.6	257.5	67.8	254.6	3.6
9	Neah Bay*	48.367	124.617	78.0	246.7	80.8	245.0	3.7
10	Mukkaw Bay	48.295	124.672	91.4	240.3	91.1	239.7	1.0
11	La Pérouse 1	48.480	125.268	87.7	235.9	89.3	236.2	1.6
12	La Pérouse 2	48.750	125.568	90.7	235.4	92.0	235.8	1.5
13	CZ3*	48.262	125.758	88.8	235.3	90.2	236.1	1.9
14	Effingham Bay*	48.875	125.307	94.0	234.6	92.7	235.2	1.6
15	Estevan 1*	49.352	126.757	97.4	238.9	95.3	239.9	2.7
16	Estevan 2*	49.270	126.878	97.3	239.4	94.5	240.0	2.9
17	Estevan 3a*	49.068	127.070	96.2	238.8	93.0	240.0	3.8
18	Estevan 5*	48.782	127.592	95.9	239.8	90.8	240.5	5.2
19	Nootka*	49.622	126.615	99.7	239.8	98.3	240.6	2.0
20	Kyuquot*	50.217	127.353	99.0	241.4	98.2	242.9	2.8
21	Brooks South	49.837	127.943	98.5	242.0	95.7	243.1	3.4
22	Brooks North	50.267	128.352	98.3	244.0	97.5	244.4	1.1
23	Hunt Islets*	50.473	128.317	101.1	243.6	98.4	244.5	3.1
24	Cape Scott	50.783	128.417	108.0	244.2	106.6	242.5	3.5
25	QC12	51.005	128.698	113.2	245.9	111.7	246.4	1.7
26	QC14	51.053	129.438	106.8	248.1	105.4	248.1	1.4
27	QC15	51.120	127.945	123.1	247.1	120.5	248.5	3.9
28	Hakai Pass	51.690	128.107	126.0	248.0	123.4	247.9	2.5
29	Port Hardy	50.717	127.483	133.0	251.9	131.5	255.0	7.3
30	Egg Island	51.250	127.833	118.1	249.0	119.8	248.3	2.2
31	Wadhams	51.517	127.517	124.7	249.0	122.8	247.8	3.3
32	G05	51.363	128.915	115.0	247.4	113.5	248.4	2.6
33	G01	51.600	128.883	119.0	249.0	118.3	249.5	1.3
34	Q05	51.367	130.017	107.9	250.5	106.7	251.0	1.5
35	QC10	51.847	129.578	120.1	251.9	119.5	251.8	0.6
36	Beauchemin Channel	52.782	129.298	145.3	253.9	143.8	252.5	3.9
37	Bella Coola	52.383	126.800	142.6	252.6	144.5	248.6	10.1
38	Bella Bella	52.167	128.133	129.7	249.8	130.3	249.0	1.8
39	Milne Island	52.617	128.767	128.2	250.7	134.3	250.2	6.2
40	McKenney Island	52.650	129.483	137.8	255.1	140.0	253.6	4.2
41	QC13	51.680	130.565	114.4	257.7	107.3	254.5	9.5
42	Fox Island	51.067	127.600	124.1	250.1	121.8	251.8	4.2
43	Q06	51.483	130.483	111.7	256.8	111.9	255.9	1.8

constituents. All of the rms amplitude differences are within 2.3 cm and, with the exception of Q_1, all rms phase differences are within 3.5 deg. Due its small magnitude, Q_1 is particularly susceptible to contamination by background noise and other tidal constituents that may not have been resolved in a time series analysis of less than six months.

The M_2 and K_1 model coamplitudes and cophases (Figs. 4a and 4b) are very similar to those in Fig. 3 of F88. Though coamplitude and cophase plots for the remaining six constituents are not shown, their relationships to M_2 and K_1 are very close to those described in FW90. Over the southern portion of the shelf, plots of the coamplitudes of the M_2 clockwise and counterclockwise velocity components are similar to Figs. 7 and 8 in FW90. In the northern region, the speeds remain small except in Queen Charlotte Sound where, consistent with Fig. 5 in Foreman et al. (1993), the clockwise component becomes as large as 30 cm s^{-1} over Cook and Goose Island Banks.

Figures 5a and 5b show K_1 clockwise coamplitude and cophase plots at 30-m depth for the southern shelf. [The clockwise component is the dominant rotary component for barotropic contintental shelf waves (Hsieh 1982; Crawford and Thomson 1984).] These figures also include values computed from historical time series at meters located between 30 and 40 m depth. Most of these observations were taken during either the Van-

TABLE 1. *Continued.*

K_1				
Observed		Model		
Amp	Phase	Amp	Phase	D
41.3	237.7	42.6	239.9	2.1
38.9	240.8	39.8	239.9	1.1
37.9	245.3	37.8	244.0	0.8
39.2	246.1	393	246.5	0.3
39.1	246.1	38.7	246.0	0.4
44.9	254.8	44.9	253.1	1.3
54.8	261.5	52.3	260.2	2.8
54.6	251.3	51.4	251.1	3.3
49.5	248.4	47.3	246.4	2.8
46.9	240.8	44.7	241.4	2.3
42.0	243.3	41.4	244.0	0.8
39.7	244.4	39.7	243.7	0.5
42.4	241.5	43.0	242.0	0.7
38.8	245.8	38.5	245.6	0.3
44.0	239.0	43.9	242.7	2.8
43.5	242.8	43.3	243.5	0.6
43.9	245.0	42.8	244.3	1.1
43.3	244.6	42.6	244.7	0.7
45.9	237.7	45.1	242.7	4.1
47.9	245.0	43.3	244.0	4.8
44.8	243.7	44.0	245.0	1.2
45.2	244.8	44.7	245.5	0.7
43.5	247.0	45.1	245.1	2.1
44.3	246.4	45.8	245.4	1.7
45.5	246.8	46.5	247.3	1.1
45.2	246.9	47.2	247.1	1.9
46.5	248.2	47.1	249.2	1.0
45.9	250.1	46.8	249.6	1.0
49.9	249.8	49.7	251.0	1.0
44.6	251.8	46.7	250.0	2.5
46.7	251.1	46.9	250.0	0.9
44.5	250.5	46.1	248.5	2.3
44.9	251.5	46.8	250.1	2.2
44.6	249.2	48.2	250.3	3.8
46.9	250.0	48.4	251.9	2.2
47.4	252.8	49.2	254.2	2.2
48.2	253.0	49.3	250.8	2.2
45.8	251.7	47.6	250.9	1.9
43.6	253.7	48.2	251.0	5.1
44.5	253.9	47.8	253.7	3.3
49.6	248.6	46.5	253.0	4.8
46.4	251.0	47.8	251.2	1.4
45.8	253.4	46.4	253.5	0.5

couver Island coastal current (VICC) experiment (Thomson et al. 1989; Hickey et al. 1991) spanning the period of June to October 1984, or the CODE-II experiment (Freeland 1988) spanning the period of March to June 1985. The model values are generally similar to those in FW90, but provide much more detail due to the finer model resolution. Qualitatively, the model amplitudes are seen to reproduce the observed values quite well. Regions with larger amplitudes are seen to correlate closely with shallow banks, whereas smaller amplitudes correlate with canyons and depressions. (Unfortunately heavy commercial fishing on most of the shallow banks precluded the successful deployment of current meters.) This is a direct consequence of the shelf

TABLE 2. Rms elevation differences at all the sites listed in Table 1 and shown in Fig. 2.

	M_2	K_1	S_2	O_1	N_2	P_1	K_2	Q_1
Amp (cm)	2.3	1.8	1.2	1.2	0.9	0.8	0.4	0.4
Phase (deg)	1.4	1.7	1.8	1.6	2.1	2.4	3.5	7.0

waves conserving potential vorticity (Gill 1982). Particles moving into shallower water acquire clockwise (negative) relative vorticity, while those moving into deeper water acquire counterclockwise (positive) relative vorticity. The model clockwise phases are seen to be reasonably accurate near the entrance to Juan de Fuca Strait but off Tofino and Estevan Point they are too small by up to 35°. These values can be compared with the F88 Table 2 results that show, for example, phase discrepancies as large as 70° off Estevan Point. (We suspect that our accuracy improvements are due to the higher resolution and better specified conditions along the forcing boundaries.) Nonetheless, even though this model is more accurate, the wavelength is still underestimated. The cross-shelf band of minimal phase values to the northwest of Juan de Fuca Canyon probably arises from scattering due to the highly irregular topography (Wilkin and Chapman 1990).

Figure 6 and Table 3 compare ''observed'' and modeled current ellipses at four representative locations in the model domain. Here M_2 and K_1 are the largest constituents in the semidiurnal and diurnal bands and, as seen in Table 3, their accuracy and trends are similar to those for lesser constituents such as S_2 and O_1. Figure 6a shows the M_2 and K_1 ellipses versus depth at site J2 (labeled 44 in Fig. 2), a VICC experiment mooring in the middle of the entrance of Juan de Fuca Strait. Large discrepancies in the M_2 phase lags at the top two moorings (and the bottom three model sigma surfaces) can be explained by the fact that the phase incurs a 180° discontinuity when the ellipse angle of inclination moves below the northern quadrant (Foreman 1978). Consequently, for the purpose of comparison with the model results, these two ''observed'' phases may be considered to equal 288° and 281°, respectively. In general, notice that both M_2 and K_1 speeds are slightly smaller than observed, and the model phase lags, though having approximately the correct values, display opposite trends down the water column from the observations.

Figure 6b shows the same ellipses at mooring A1 (45 on Fig. 2), a location along the shelf break that has been used to delineate seasonal changes in upwelling and the Shelf Break Current (Thomson and Ware 1996). The mooring has been in place since 1985 and the ellipse parameters shown here are averages of yearly analyses of near continuous records collected from 1990 to 1995. The highly variable ''observed'' M_2 parameters suggest the presence of internal tides similar to those observed and analyzed by Drakopoulos and Marsden (1993). These cannot be represented with the present barotropic

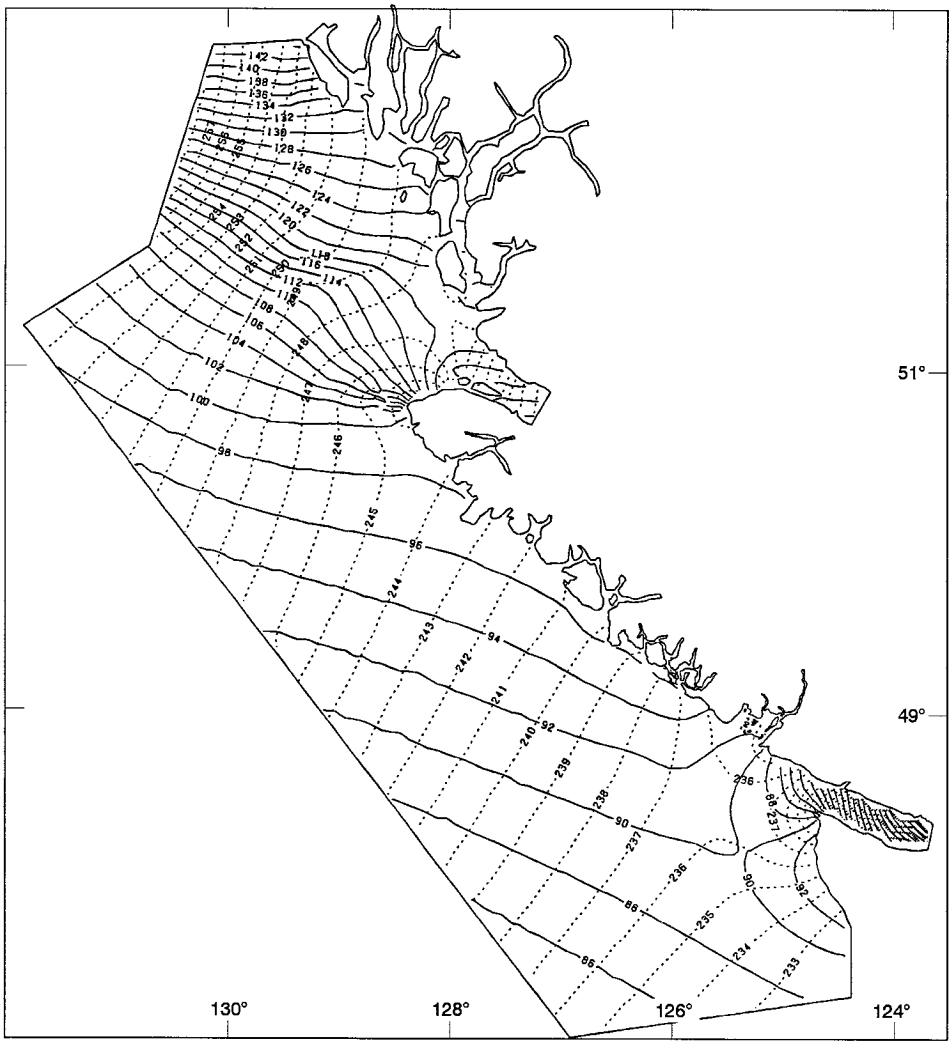

FIG. 4. Model coamplitudes (cm) (solid) and cophases (deg UTC) (dashed) for (a) M_2 and (b) K_1.

model. The model-versus-observed comparison for K_1 is also unsatisfactory. The model ellipses are too large and do not display the same magnitude decrease and rapid transition in phase lag with depth that is evident in the observations. Although this may be partially due to an inappropriate vertical viscosity parameterization, it is more likely due to the presence of a baroclinic velocity component (Crawford and Thomson 1984; Crawford 1984) that the model cannot capture. However, as the amplitude of the clockwise rotary component does change rapidly near A1 (Fig. 5a), the large model speeds might also be due to insufficient grid resolution in this region.

Figure 6c shows tidal ellipses at site T4 (site 46 in Fig. 2), another VICC experiment mooring. The K_1 speeds here are only slightly larger than the observations and provide a much better representation of, what now appear to be, barotropic variations in the observations down the water column. However, the model phase lags are too large by 17° at 30-m depth, by 24° at 50 m, and by 34° at 100 m. In the context of Fig. 5b, this implies that not only is the model wavelength too short, but also it is slightly later with depth, a result that is opposite to the trend indicated by the observations. A similar pattern is evident with O_1 (see Table 3) where the model phase lags are too large by 17°, 32°, and 46° at the same respective depths. The M_2 model currents are generally smaller than those measured and their phases again display the wrong trend with depth. As with site 45, the anomalous ''observed'' ellipse at 30 m suggests the presence of internal tides.

Finally Fig. 6d shows the tidal ellipses at site E01 (47 in Fig. 2) off Estevan Point. This mooring also has a multiyear time series. Calculated ellipses are averages from yearly analyses between 1990 and 1995. The top M_2 observed ellipse is reasonably well represented by the model while the lower ellipse is close to the bottom and does not correspond well with the ''observation.''

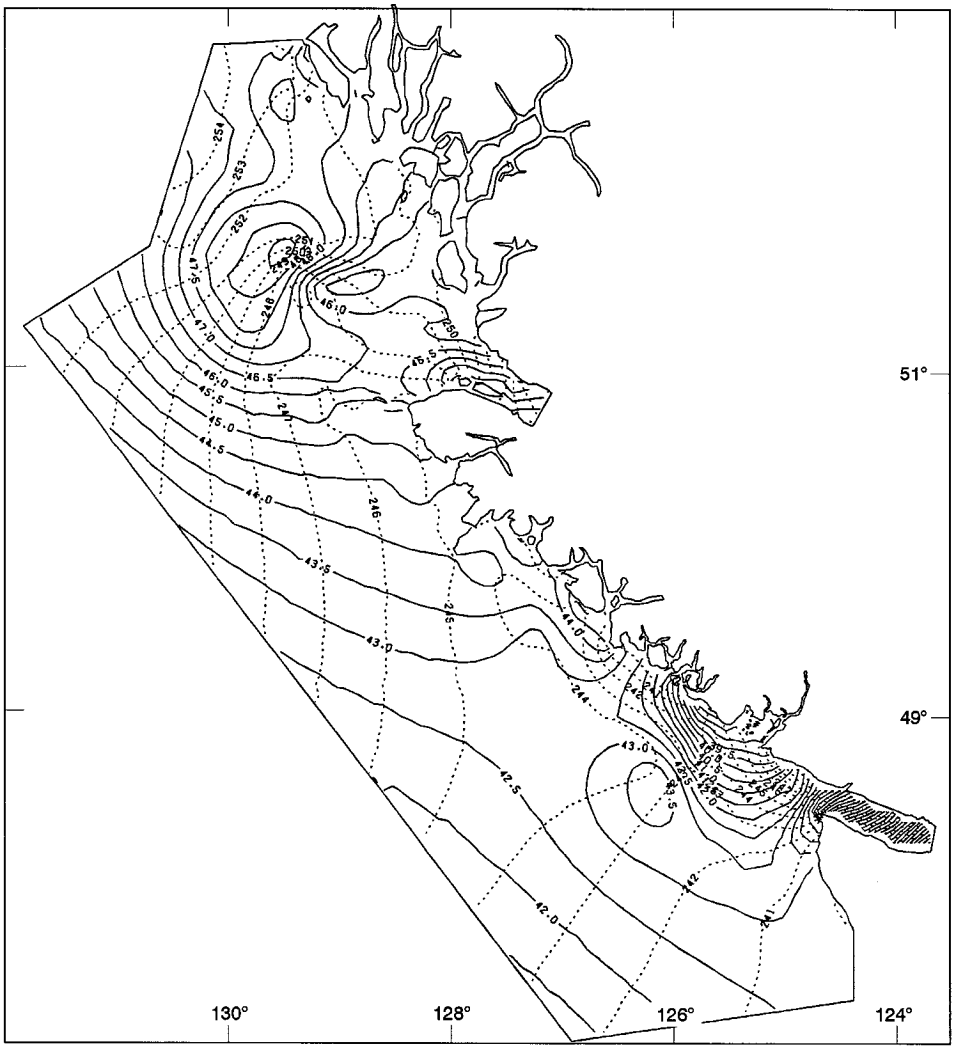

FIG. 4. (*Continued*)

The K_1 model speeds are quite accurate near the surface but too small at depth. Consistent with the results at VT4, the observed diurnal currents appear to be barotropic and the model phase lags too large by about 40°. However, this is better than the 72.5° discrepancy shown in Table 2 of F88. Again O_1 displays similar behavior to K_1. However, its phase lags are too large by 43° and 50° at depths 35 and 75 m, respectively.

4. Shelf wave experiments

By artificially blocking the entrance to Juan de Fuca Strait, Flather (1988) reduced his model K_1 speeds by a factor of 5 along the Vancouver Island shelf. This effectively demonstrated that the shelf wave arises almost solely from oscillatory flows in the strait. We confirmed this result with a slightly different experiment that removed all boundary forcing except for the velocities in Juan de Fuca Strait. In particular, the elevation forcing on the northern, southern, western, and Queen Charlotte Strait boundaries was replaced with directional boundary conditions. Flow along the Queen Charlotte Strait boundary was constrained to be normal to the boundary, flow along the western boundary was constrained to be tangential (this is the same condition that is used along the coast), and flow along the northern and southern boundaries was constrained to be in the same northwesterly direction as for the western boundary. In order to permit a solution to the wave equation with this set of Neumann conditions, it was necessary to have at least one specified elevation on the boundary (i.e., one Dirichlet condition). This was accomplished by setting the elevation of the node at the northwest corner of the grid (farthest from Juan de Fuca Strait) to be zero.

South of Brooks Peninsula, the K_1 clockwise amplitudes arising from this run (Fig. 7) were virtually identical to those of Fig. 5a. The clockwise phases (not

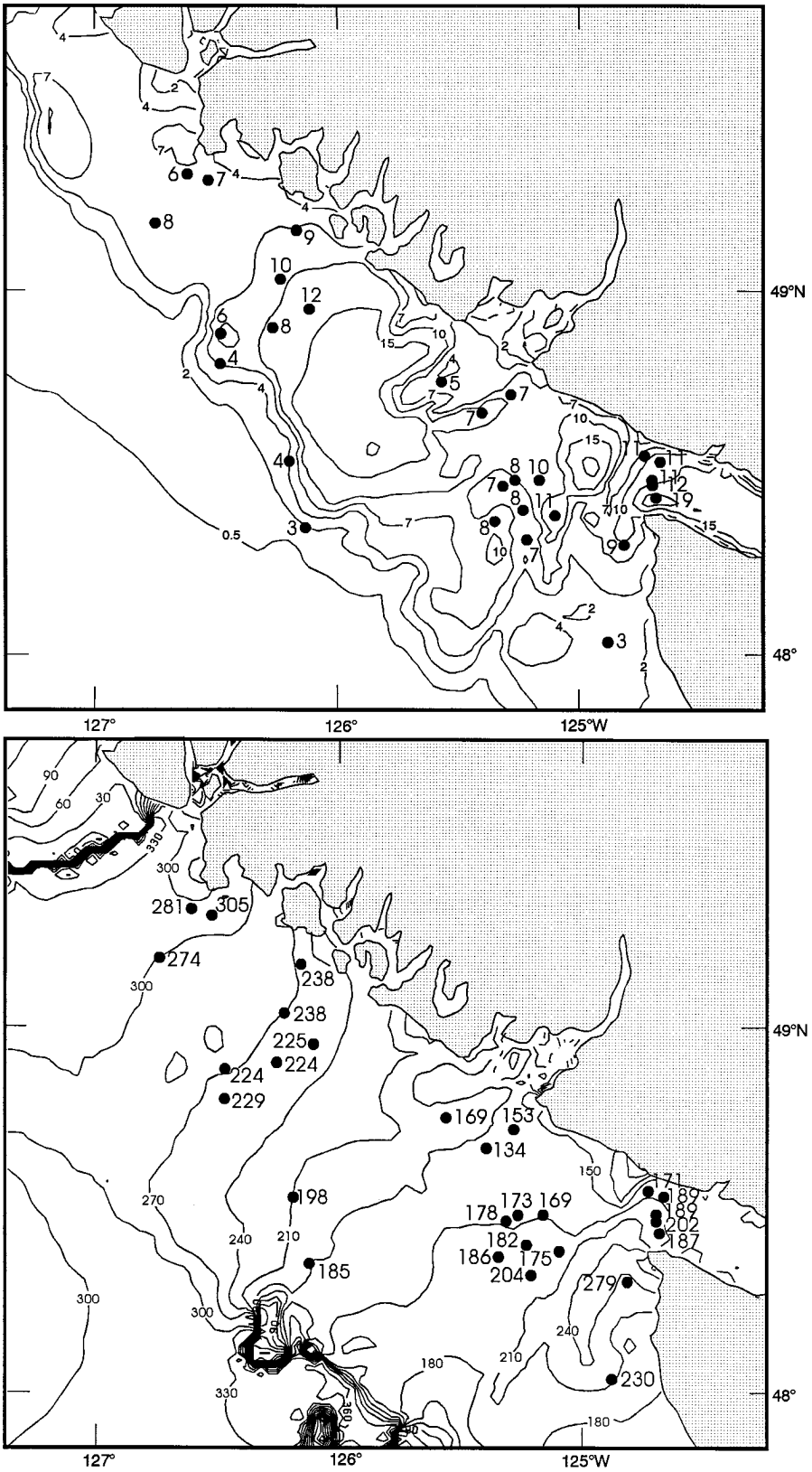

FIG. 5. The K_1 clockwise (a) coamplitude (cm s^{-1}) and (b) cophase (deg UTC) contours at 30-m depth for the southern shelf with model forcing on all sea boundaries. Asterisks and labels denote locations and values computed from historical time series at meters located between 30-m and 40-m depth.

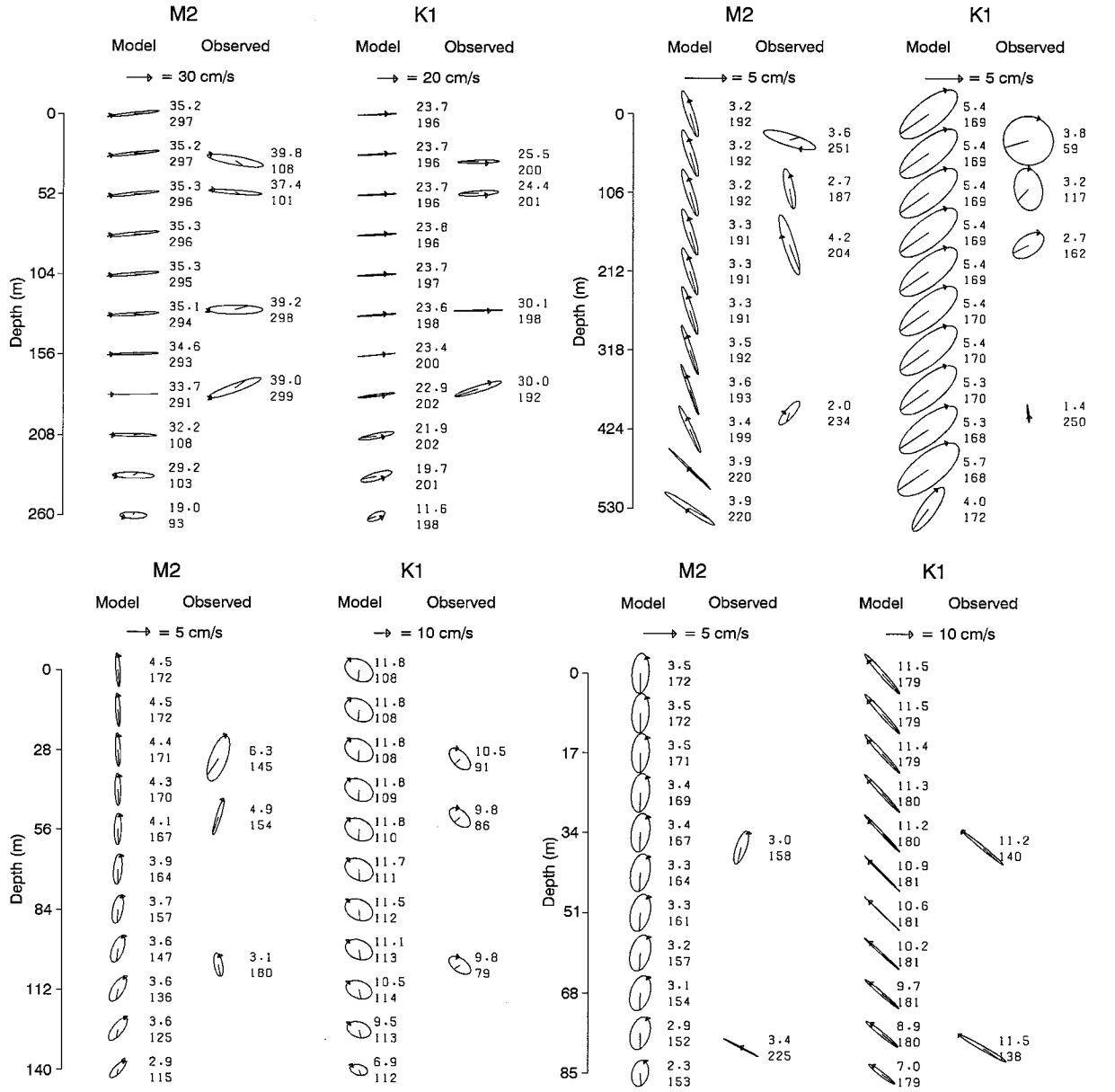

FIG. 6. The M_2 and K_1 current ellipses at sites (a: top left) J2, (b: top right) A1, (c: bottom left) T4, and (d: bottom right) E01. The line within each ellipse denotes G, the position of the current vector at the time of maximum tidal potential at Greenwich, and the arrow denotes the sense of rotation. The two numbers beside each ellipse are the major semiaxis (top, in cm s^{-1}) and G (bottom, in deg UTC).

shown) were also virtually identical to those in Fig. 5b. This confirms Flather's (1988) conclusion that flows in Juan de Fuca Strait are almost solely responsible for the generation of the diurnal shelf waves. In this model, the Juan de Fuca Strait flows are the sole generation mechanism for the clockwise component of the K_1 speeds on the southern shelf. (A similar experiment with only O_1 forcing in Juan de Fuca Strait produced analogous results.) Furthermore, the fact that very little of the energy in this clockwise component makes it past Brooks Peninsula suggests that this promontory might be a barrier to the Vancouver Island shelf waves. Certainly, the large K_1 speeds observed in Queen Charlotte Sound cannot be attributed to the shelf waves generated in Juan de Fuca Strait.

To better understand the role of Brooks Peninsula in the northwesterly propagation of these waves, the model grid was modified by replacing the peninsula with a coastline and bathymetry contours that were smooth extensions of those to the northwest and southeast. The previous experiment with K_1 forcing only in Juan de Fuca Strait was repeated and, to our initial

TABLE 3. The O_1, K_1, M_2, and S_2 tidal current ellipse parameters for the same locations shown in Fig. 6. Depths are in meters, major and minor semi-axes are in centimeters per second, and angle of inclination and Greenwich phase lag (UTC) are in degrees.

			Observed				Modeled			
Site	Depth	Constituent	Major	Minor	Inclin	Phase	Major	Minor	Inclin	Phase
J2	30	O_1	13.0	1.0	11	176	12.7	−1.2	5	173
		K_1	25.5	2.1	2	200	23.7	−.5	3	196
		M_2	39.8	−6.1	170	108	35.2	−1.8	6	297
		S_2	10.3	−.7	169	131	9.1	−.7	5	319
	50	O_1	12.8	1.3	19	177	12.6	−1.2	5	173
		K_1	24.6	3.1	4	201	23.7	−.6	3	196
		M_2	40.0	−3.0	176	107	35.3	−1.9	6	296
		S_2	12.9	−2.5	173	127	9.0	−.7	5	319
	125	O_1	15.4	−.8	7	173	11.9	−.8	5	175
		K_1	30.1	0.5	1	198	23.6	−.6	4	198
		M_2	39.2	6.4	0	298	35.1	−1.9	3	294
		S_2	9.8	1.2	175	140	8.9	−.5	2	317
	175	O_1	17.5	−5.6	1	167	10.9	.9	6	177
		K_1	30.0	−3.7	8	192	22.9	1.2	8	202
		M_2	39.0	5.8	20	299	33.7	−.1	0	291
		S_2	9.6	1.3	18	327	8.4	.0	0	314
A1	35	O_1	1.9	−1.7	15	155	1.6	−.9	69	118
		K_1	3.8	−3.7	138	59	5.4	−2.1	39	169
		M_2	3.6	−.8	163	251	3.2	.5	108	192
		S_2	1.4	−.3	117	236	1.3	−.1	93	208
	100	O_1	1.5	−1.1	89	97	1.6	−.9	69	118
		K_1	3.2	−2.1	99	117	5.4	−2.1	39	169
		M_2	2.7	0.6	103	187	3.2	.5	108	192
		S_2	0.6	0.2	132	245	1.4	−.1	93	208
	175	O_1	1.5	−.6	34	140	1.7	−.9	69	118
		K_1	2.7	−1.5	37	162	5.4	−2.1	39	169
		M_2	4.2	−.7	107	204	3.3	.5	108	191
		S_2	0.7	.0	140	254	1.4	−.1	93	208
	400	O_1	1.2	.1	87	225	1.5	−.5	76	132
		K_1	1.4	.1	97	250	5.3	−2.0	38	168
		M_2	2.0	−.6	50	234	3.4	.3	114	199
		S_2	0.5	.0	97	196	1.3	.0	107	223
T4	30	O_1	5.3	−3.0	133	63	7.0	−5.2	136	80
		K_1	10.5	−5.7	133	91	11.8	−8.2	151	108
		M_2	6.3	−2.2	70	145	4.4	.6	92	171
		S_2	3.6	−2.2	58	182	1.5	.2	103	207
	50	O_1	5.1	−2.9	138	50	6.9	−5.2	137	82
		K_1	9.8	5.6	138	86	11.8	−8.2	152	110
		M_2	4.9	−.6	74	154	4.1	.9	89	167
		S_2	2.6	−1.2	92	201	1.4	.3	98	203
	100	O_1	4.7	−2.5	144	40	6.6	−4.9	141	86
		K_1	9.8	−5.2	144	79	11.1	−7.4	156	113
		M_2	3.1	1.1	101	180	3.6	1.5	69	147
		S_2	1.7	−.3	171	262	1.2	.5	71	175
E01	35	O_1	5.5	−0.3	143	106	7.1	−.1	137	149
		K_1	11.2	−0.7	141	140	11.2	−.5	133	180
		M_2	3.0	0.9	71	158	3.4	1.6	81	167
		S_2	0.8	0.3	85	196	1.2	.5	98	205
	75	O_1	5.8	−0.6	150	99	5.6	.8	146	149
		K_1	11.5	−.9	150	138	8.9	.9	141	180
		M_2	3.4	0.1	153	225	2.9	1.6	73	152
		S_2	0.6	0.2	51	138	1.0	.6	91	191

surprise, the amplitude and phase patterns changed only slightly. An explanation for this result follows in the next section.

In order to discover if the oscillatory flows in Queen Charlotte Strait play a similar role to those in Juan de Fuca Strait by generating the large diurnal speeds around Goose Island Bank, the foregoing experiment was repeated with velocity forcing in that strait, normal boundary conditions in Juan de Fuca Strait, and the same directional conditions along the other boundaries. In this case, the boundary node where the elevation was set to zero was chosen to be at the southwest corner of the grid. The results, shown in the Fig. 7 insert, indicate that the large diurnal speeds over Goose Island Bank

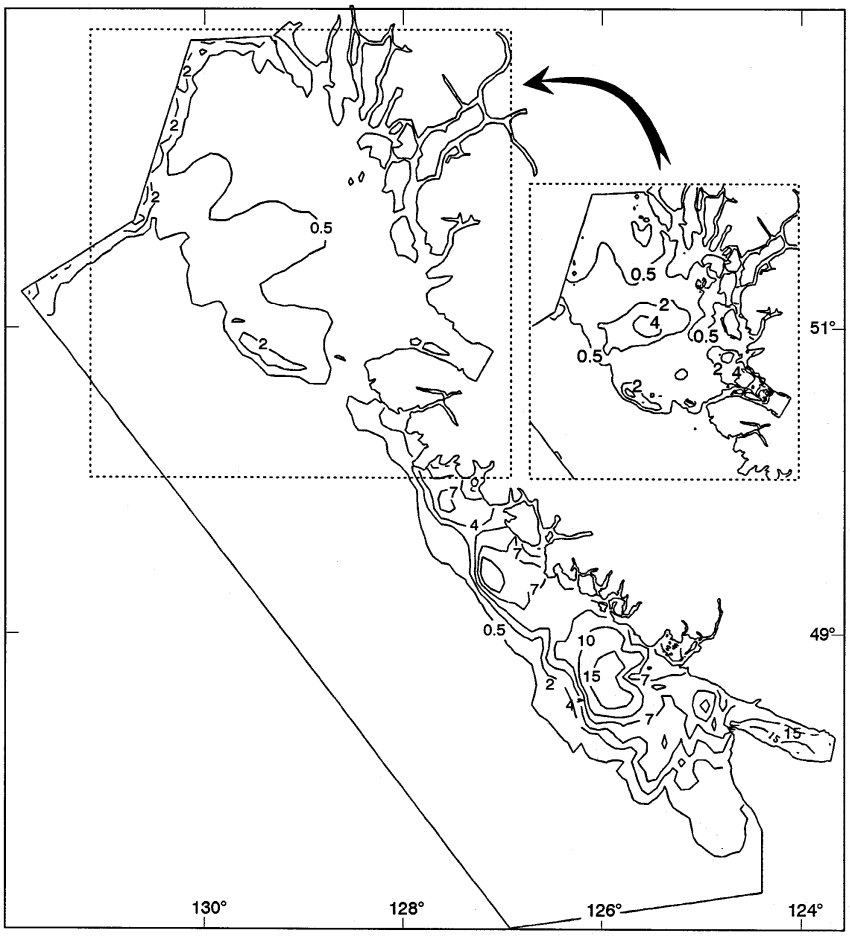

FIG. 7. As in Fig. 5a but with forcing only in Juan de Fuca Strait. Insert is with forcing only in Queen Charlotte Strait.

do not arise in a manner similar to the speeds found over Swiftsure and La Pérouse Banks. This is consistent with the Willmott and Thomson (1994) conclusion that diurnal forcing in Queen Charlotte Strait should not generate shelf waves. Energy radiating in from the open sea boundaries must therefore be necessary to generate these currents.

An interesting observation arising from the Juan de Fuca Strait experiment is the differing behavior of the clockwise and counterclockwise K_1 flows. Since the width of Juan de Fuca Strait is much less than the (barotropic) Rossby radius of deformation, K_1 flows in the strait are essentially rectilinear. This means that the clockwise and counterclockwise components are approximately equal. However, once these flows move beyond the entrance of the strait, the Rossby radius contraint necessitating their equivalence is removed. (Only along the coastal boundary where the flows are restricted to be tangential do the two rotational components remain equal.) The model results show that the counterclockwise component decreases rapidly while the clockwise speeds are preserved through the conservation of potential vorticity. This suggests that the large diurnal clockwise currents observed off Vancouver Island are not simply ''generated'' at the entrance of Juan de Fuca Strait, but rather they are conserving the large diurnal potential vorticity that already exists in the strait. (Model-derived potential vorticity contours for both K_1 and M_2 show reasonably accurate, but not perfect, conservation.) The clockwise component is enhanced because the shelf region is shallower than typical depths in Juan de Fuca Strait, whereas the counterclockwise component dies away.

In an attempt to discern the roles of Swiftsure Bank and Nitinat and Barkley Canyons in the generation and propagation of the shelf wave, we artificially adjusted these bathymetric features. In separate studies, the canyons were filled in and the steep sides of Juan de Fuca Canyon and Swiftsure Bank were flattened. Consistent with the argument that the shelf waves are merely conserving potential vorticity already present in Juan de Fuca Strait, these bathymetric changes caused only local modifications to the speeds and phases of the shelf

waves. There were virtually no changes farther upstream.

5. Buoyancy-driven currents and their interaction with the shelf waves

Summer and winter buoyancy-driven currents within the model domain were calculated in a manner similar to that described in Ballantyne et al. (1996), Foreman et al. (1992), and Naimie et al. (1994). In addition to the specification of a stationary three-dimensional density field as required by term **b** in Eqs. (3) and (7), it is important to note that this calculation also involves two links to the tidal currents whose calculation has been described previously. The first link is that both the quadratic bottom friction and vertical eddy viscosity terms include the bottom tidal velocities. This ensures the correct frictional dissipation for the buoyancy flows. The second is that both the advective terms in the momentum equations and the wave-drift term in the continuity equation include the three-dimensional tidal velocities. This means that the calculated seasonal buoyancy flows also include the effects of tidal rectification. Although wind stress has not been explicitly included along with the buoyancy forcing, its effects on the observed density field imply an indirect inclusion. As with the calculation of tidal currents, the buoyancy-driven currents represented here do not include a stratification-dependent vertical viscosity. Preliminary tests indicate that such a dependency does change both the tidal and background currents profiles [consistent with the results of Davies (1993) and Soulsby (1990)] but does not, in general, produce more accurate currents when compared with current meter observations.

The seasonal flow fields presented here are to be viewed as typical for the purpose of sensitivity studies, rather than climatological averages of the type computed by Naimie et al. (1994). The 3D summer σ_t field was calculated from an objective analysis (Denman and Freeland 1985) of conductivity and temperature versus depth (CTD) measurements collected primarily in June 1984 and July 1995 off the western and northern coasts of Vancouver Island. These two particular cruises were chosen because they had virtually no spatial overlap and because together they provided a reasonably dense sampling of the model domain (Fig. 8a). The correlation ellipse for the objective analysis was chosen to be inclined at 45° counterclockwise from the north with major and minor semiaxes of 50 km and 25 km. As seen in Fig. 8a, the smoothness of the resultant sigma-t field at 50-m depth demonstrates that there is no apparent misfit between the two distinct sets of observations. Although the horizontal CTD coverage encompassed the model domain, the vertical coverage only extended to 1000 m. Contributions to the baroclinic pressure gradient below this depth were assumed to be zero and this did not seem to cause any numerical difficulties.

The winter σ_t field was computed from CTD observations taken in January 1980 and March 1994 (Fig. 8b). [The location of the 1980 CTD stations are also shown in Thomson et al. (1989).] Again there was little spatial overlap between the two cruises but due to a much larger separation of the CTD stations, the correlation ellipse had to be given major and minor semiaxes lengths of 140 and 50 km. The objectively analyzed sigma-t field at 50-m depth (as seen in Fig. 8b) is again very smooth. For both seasonal simulations, elevation-specified boundary conditions that provided outflow in Juan de Fuca Strait and no geostrophic bottom flow normal to the boundary [analogous to those described in Naimie et al. (1994) and Ballantyne et al. (1996)] were used.

Figures 9a and 9b show the seasonal model flows at 30-m depth with Fig. 9c demonstrating that the contribution from tidal rectification is generally quite small. The summer pattern is similar to that displayed in Fig. 4 of Foreman et al. (1992) and Fig. 11 of Thomson et al. (1989). The buoyancy-driven Vancouver Island Coastal Current flows northwestward while the shelf break current, whose forcing in this model simulation arises indirectly through the impact of wind stress on the density field, is seen to flow in a southeasterly direction. The model summer flows are also seen to agree qualitatively with the low-pass filtered VICC observations shown in Fig. 5 of Foreman et al. (1992).

The winter flow pattern, shown in Fig. 9b, is much simpler. The buoyancy-driven VICC and wind-driven shelf break current both flow to the northwest. Apart from some topographically induced meanders, they are in reasonable agreement with the low-pass filtered observations shown in Thomson et al. (1989).

Flather (1988) demonstrated that the K_1 shelf wave wavelength increases in the presence of model flows arising from a 0.23 N m^{-2} wind stress from the southeast. His model flows were compared with selected current meter observations taken in 1979 and 1980. On the basis of multiyear time series at sites E01 and A1 we now provide a more quantitative evaluation of this seasonal behavior. (For these analyses, summer was defined to be June through August inclusive, while winter was defined to be December through February.) Tables 4 and 5 show the results of experiments similar to Flather's in which the tidal flows interacted with the previously described buoyancy flows. Table 4 shows the E01 average summer and winter major semiaxis speeds and phase lags along with their standard deviations, while Table 5 shows similar statisitics for the clockwise current component amplitudes and phases at A1. (The K_1 ellipses are almost circular at A1 making the definitions of major semiaxis and phase lag nonrobust.) Although there are only small seasonal changes in the observed speeds at E01, the observed phases are seen to increase by 24° from summer to winter at 35-m depth and by 16° at 75 m. The model results are seen to exhibit similar phase shifts of 28° and 27°, respectively, but much larger decreases in speed.

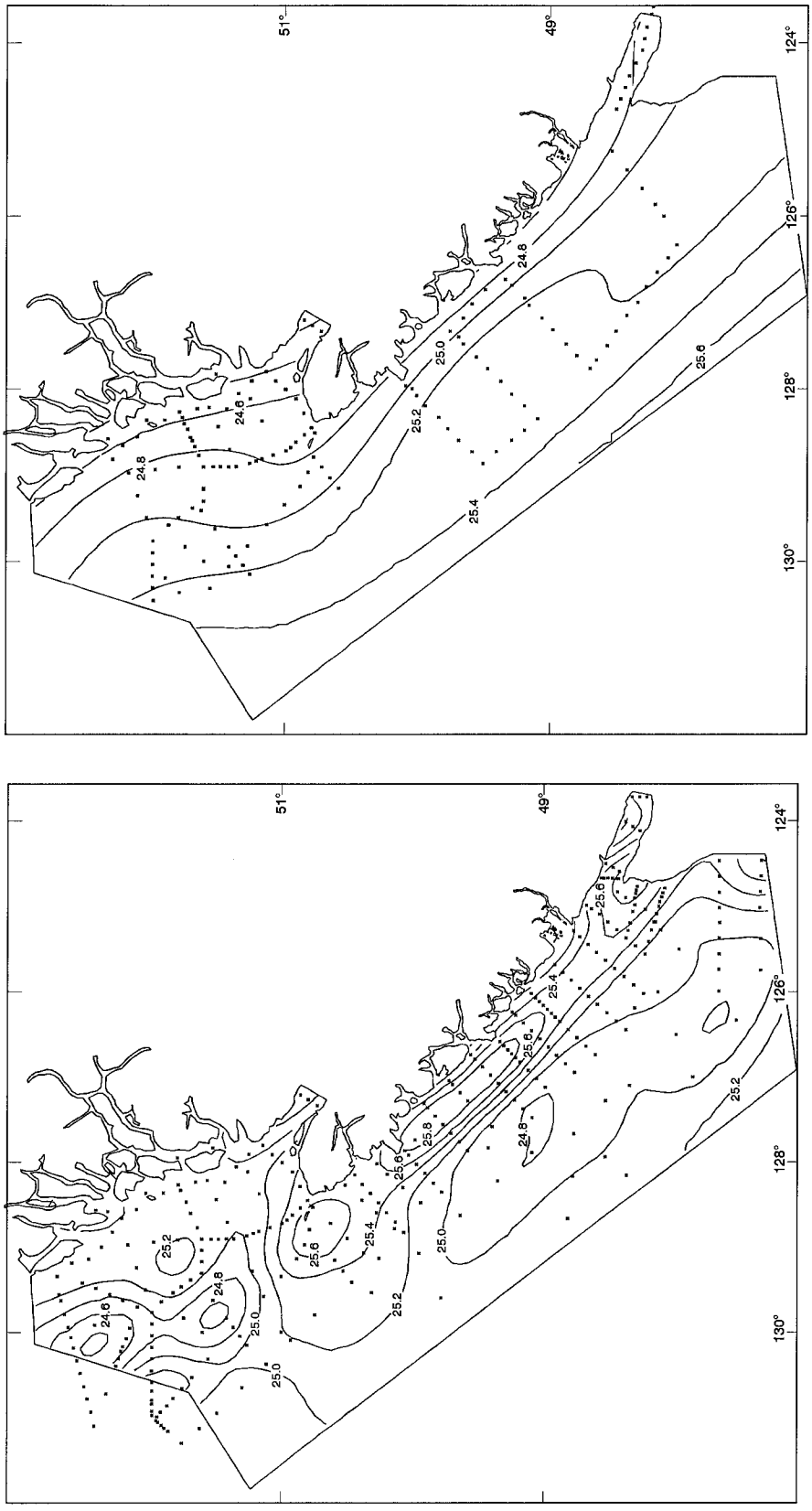

FIG. 8. Sigma-t fields at 50-m depth as calculated from the objective analysis of CTD data from (a) the summer cruises and (b) the winter cruises. CTD stations are shown as solid boxes.

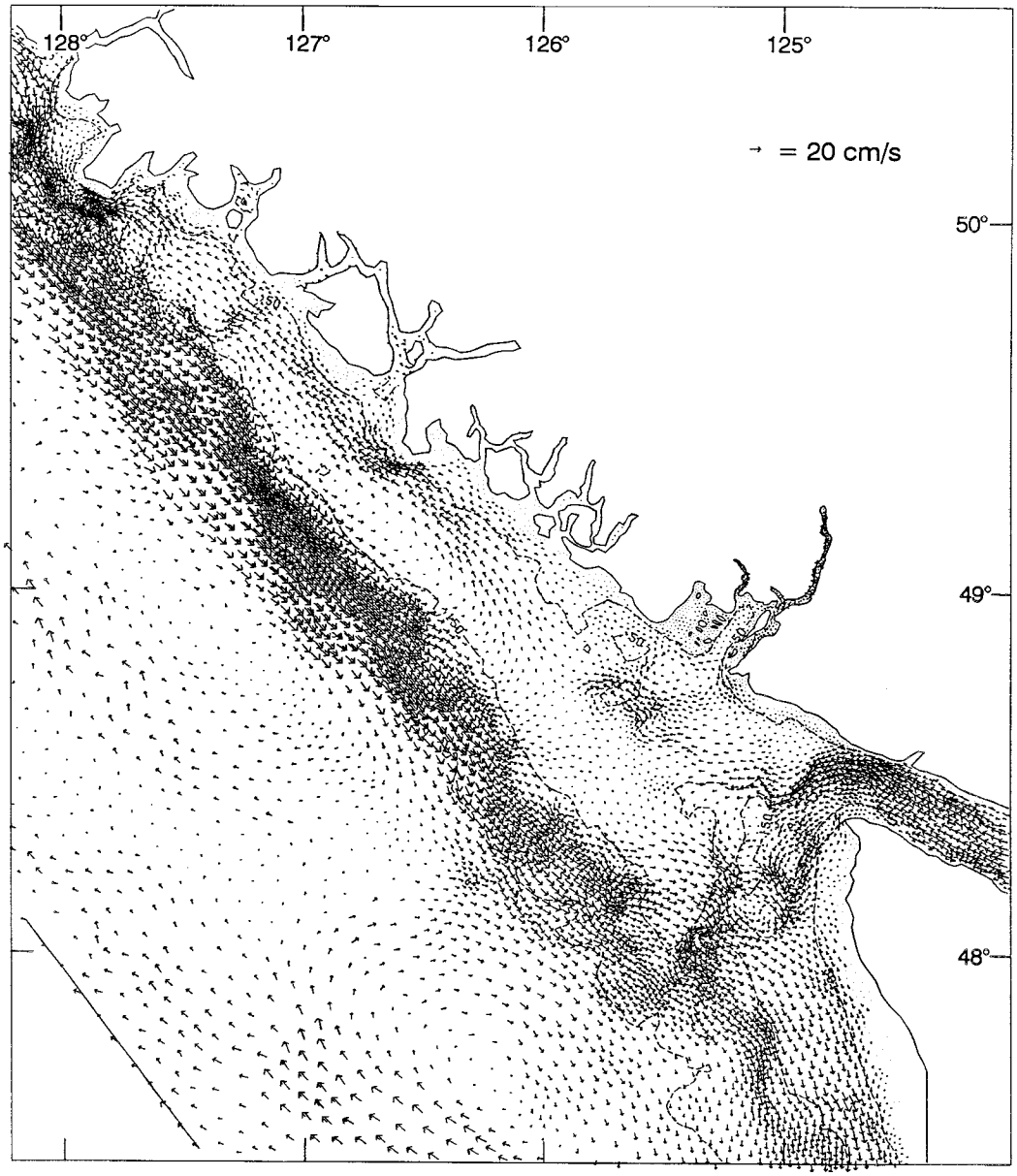

FIG. 9. Combined buoyancy-driven and tidally rectified currents at 30-m depth for selected (a) summer and (b) winter forcing. Each full shaft in multishafted vectors represents 20 cm s^{-1}. The contribution from only the tidally rectified currents is shown in (c) with different scaling.

At mooring A1, the model phase shifts are much larger that those arising from the observations. In fact, the latter do not appear to display any significant seasonal shift. We can only speculate on the poor model performance here. As the initial model K_1 representation at A1 (see Fig. 6c) was poor due to a lack of baroclinicity, it is suspected that a more accurate simulation of the seasonal behavior will have to wait for a fully baroclinic model. It may be that seasonal variations in the bed friction due to the presence of internal tides are as important as the advective interactions studied here. Furthermore, although both the analytical model studies of Crawford and Thomson (1984) and some preliminary tests that we performed suggest otherwise, seasonal variations due to a stratification-dependent vertical eddy viscosity may also prove to be important with the fully baroclinic model simulations.

A close inspection of the K_1 clockwise model phases for winter shows that, in fact, the phase shift is largest off Estevan Point. The speeds and phases change very little over La Pérouse Bank, but a local minimum in the speeds that originates over Clayquot Canyon in the summer (and in the seasonally independent run shown in Fig. 5a) extends to the northwest to Estevan Point in

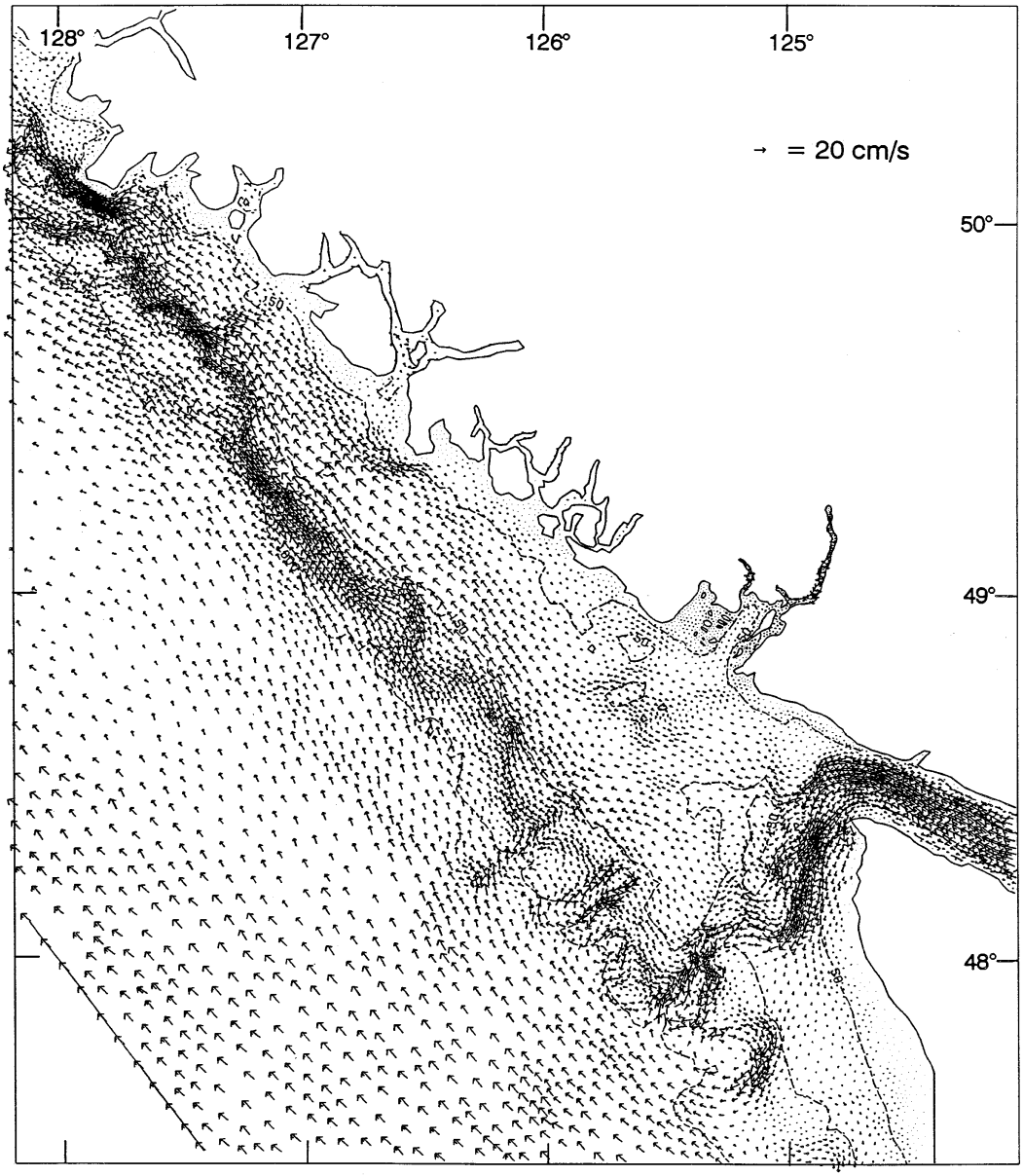

FIG. 9. (*Continued*)

the winter. A similar minimum that overlays Nitinat Canyon in Fig. 5a also extends much farther into the shelf region in the winter. The net result seems to be that the winter buoyancy flows have shifted the K_1 wavelength so that its natural nodes correspond better with the spacing of canyons along the shelf break. Inspection of the counterclockwise components reveals much smaller differences between the winter and summer amplitudes and phases.

This phenomenon of seasonal shifts in these diurnal currents is analogous to the seasonal shifts in the M_2 degenerate amphidrome off Victoria (Foreman et al. 1995) and the M_2 amphidrome in Tsushima Strait (Kang et al. 1995). The most sensitive locations for these shifts are, not surprisingly, near the minimal tidal values. Model runs that included the seasonal buoyancy flows in only the bottom friction and vertical viscosity terms, but not the advective and wave drift ($\eta\mathbf{u}$) terms, displayed virtually no change from the seasonally independent results. Subsequent tests also confirmed that the wave drift contribution is insignificant. Consequently, it is the advective interaction of the K_1 tidal constituent with seasonal buoyancy flows that causes the seasonal shift in wavelength. In essence, this is a Doppler shift phenomenon. The K_1 phase velocity of about 3 m s^{-1} to the northwest is shifted by approximately $\pm 5\%$ due to a Shelf Break Current that varies seasonally by ± 0.15 m s^{-1}.

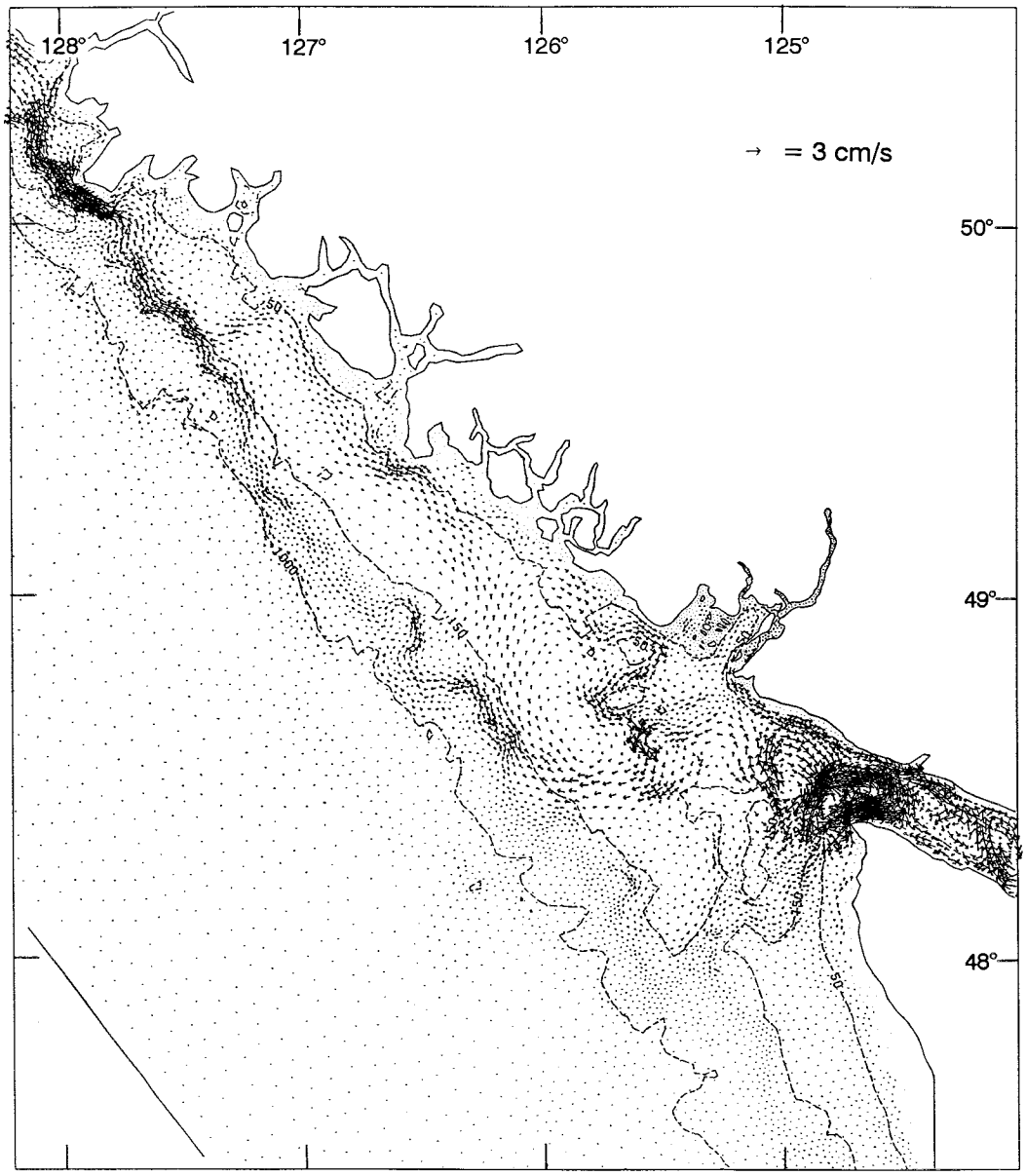

FIG. 9. (*Continued*)

Although analogous numerical experiments were not performed to study seasonal shifts in the wavelength of O_1 and the other diurnal constituents, the analyses of Crawford and Thomson (1984) lead us to suspect that the results from such runs would be similar to those just reported for K_1.

6. Energy flux and power estimates

Additional insight on the diurnal shelf waves can be provided through an analysis of their energy and power characteristics. The vertically integrated energy flux (Henry and Foreman 1977; Kowalik and Proshutinsky 1993) is given by

$$\mathbf{F} = (H + \eta)\rho\left[\frac{1}{2}|\bar{\mathbf{u}}|^2 + g\eta\right]\bar{\mathbf{u}}, \tag{11}$$

where ρ ($=1025$ kg m^{-3}) is a representative seawater density. Although the kinetic energy contribution in this expression is often neglected due to domination by the potential energy, the surface elevation η associated with shelf waves is small. Consequently the energy flux calculations presented here include both contributions in (9).

Figures 10a and 10b show the K_1 and O_1 vertically integrated energy flux vectors, averaged over one tidal cycle, arising from the model runs with forcing only in Juan de Fuca Strait. Figure 10a can be compared with

TABLE 4. Comparison of model and observed K_1 major semiaxes (cm s^{-1}) and phases (deg UTC) at station E01. Observed values are averages and standard deviations between 1990 and 1995. The ''no season'' observed values are from yearly analyses, whereas ''no season'' model values do not include any seasonal interactions with buoyancy or wind-driven flows.

		Observed		Model	
Depth		Major	Phase	Major	Phase
35 m	no season	11.2	140	11.2	180
	winter	11.6 ± 1.5	128 ± 5	6.4	141
	summer	12.5 ± 0.5	152 ± 6	10.9	169
	difference	0.9	24	4.5	28
75 m	no season	11.5	138	8.9	180
	winter	11.1 ± 1.4	129 ± 3	5.4	140
	summer	13.0 ± 1.2	145 ± 6	8.6	167
	difference	1.9	16	3.2	27

TABLE 5. Comparison of model and observed K_1 clockwise current amplitudes (cm s^{-1}) and phases (deg UTC) at station A1. Observed values are averages and standard deviations between 1990 and 1995. The ''no season'' observed values are from yearly analyses, whereas ''no season'' model values do not include any seasonal interactions with buoyancy or wind-driven flows.

		Observed		Model	
Depth		Ampitude	Phase	Amplitude	Phase
35 m	no season	3.7	197	5.4	169
	winter	4.1 ± 0.1	195 ± 3	5.7	126
	summer	3.3 ± 0.4	199 ± 3	6.7	164
	difference	−0.8	4	1.0	38
100 m	no season	2.7	216	5.4	169
	winter	3.4 ± 0.4	191 ± 1	5.7	130
	summer	2.6 ± 0.3	195 ± 7	5.8	159
	difference	−0.8	4	0.1	24
175 m	no season	2.1	199	5.4	169
	winter	2.5 ± 0.3	197 ± 4	5.9	132
	summer	1.7 ± 0.1	201 ± 6	4.8	152
	difference	−0.8	4	−1.1	20
400 m	no season	0.7	347	5.3	168
	winter	0.8 ± 0.2	333 ± 11	8.1	132
	summer	0.5 ± 0.3	5 ± 12	4.7	145
	difference	−0.3	32	−3.4	13

Fig. 4 in Crawford (1984) and Fig. 6 in F88, although it is important to note that both these published figures show the combined flux from both shelf and Kelvin waves. The most notable difference among these plots is that F88 shows a combined flux into Juan de Fuca Strait when the Kelvin wave is included in the calculation, while Fig. 10a shows a flux out of the strait when there is only forcing in the strait. This suggests that the shelf wave energy emerging from Juan de Fuca Strait is probably generated through a conversion of the Kelvin wave energy that enters the strait. The processes underlying this conversion clearly warrant further investigation but are beyond the scope of this study.

The presence of several eddies in both Fig. 10 fields suggests trapping of the energy flux in energy ''sinks'' along the shelf break. This implies that although the shelf wave has phase propagation to the northwest, its energy propagation (and group velocity) along the continental slope is essentially zero. With reference to the dispersion curves shown in Fig. 8 of Crawford and Thomson (1984) and Fig. 10.17 of Gill (1982), this means that these waves are near their peak frequency. Notice that Fig. 10b shows an additional eddy for O_1 just north of the point where Juan de Fuca Canyon merges with the continental slope.

It is interesting to notice that in both energy flux plots, the cross-shelf transport associated with the eddies often corresponds with shelf break canyons. For example, K_1 has strong on-shelf fluxes approximately centered over Clayquot and Nootka Canyons and offshore fluxes through Barkley Canyon. Future particle tracking experiments will reveal whether or not these cross-shelf exchanges are relevant to larvae retention and nutrient supply issues.

Tables 6 and 7 evaluate the K_1 and O_1 power leaving Juan de Fuca Strait and in each of the eddies by integrating the energy flux along the transects shown in Figs. 10a and 10b. (The difference between the power crossing the two transects in eddy 1 gives some indication of the accuracy in this calculation.) Notice that the summation of the power in the first three K_1 eddies along the shelf break is very close to the power emanating from Juan de Fuca Strait. This explains why the removal of Brooks Peninsula in an earlier numerical experiment had virtually no effect on the K_1 clockwise currents farther upstream. Although Brooks Peninsula does impede some of the shelf wave propagation to the northern end of Vancouver Island, our budget analysis suggests that there is very little energy left in these waves by the time they reach Brooks. This energy loss is primarily due to bottom frictional dissipation en route and occurs mostly in three trapped eddies. In a steady-state balance, the tidally averaged energy cannot increase with time. Consequently, if these eddylike regions are indeed sinks for the shelf-wave energy flux, they must also coincide with regions of enhanced dissipation. Assuming that the K_1 shelf wave power can be expressed in the form A_0e^{-ky} with y being the northwesterly distance from the entrance of Juan de Fuca Strait, a simple least squares fit to the power estimates in Table 6 yields $A_0 = 107.5$ MW and $k = 0.0117$ km^{-1}.

A similar power budget holds for O_1. In this case there are four eddies along the shelf break and the summation of the power in each is slightly larger than the energy emanating from Juan de Fuca Strait. Part of this discrepancy may be attributed to the fact that some of the power crossing transects 3 and 4 in eddy 2 is leaking to eddy 1 and is counted twice. Although this power discrepancy and the existence of the additional eddy complicates the e-folding calculation slightly, a least squares fit to the O_1 shelf wave power estimates in Table 7 yields $A_0 = 29.8$ MW and $k = 0.0092$ km^{-1}.

It should be noted that the total energy flux associated with the diurnal tides along the Vancouver Island shelf

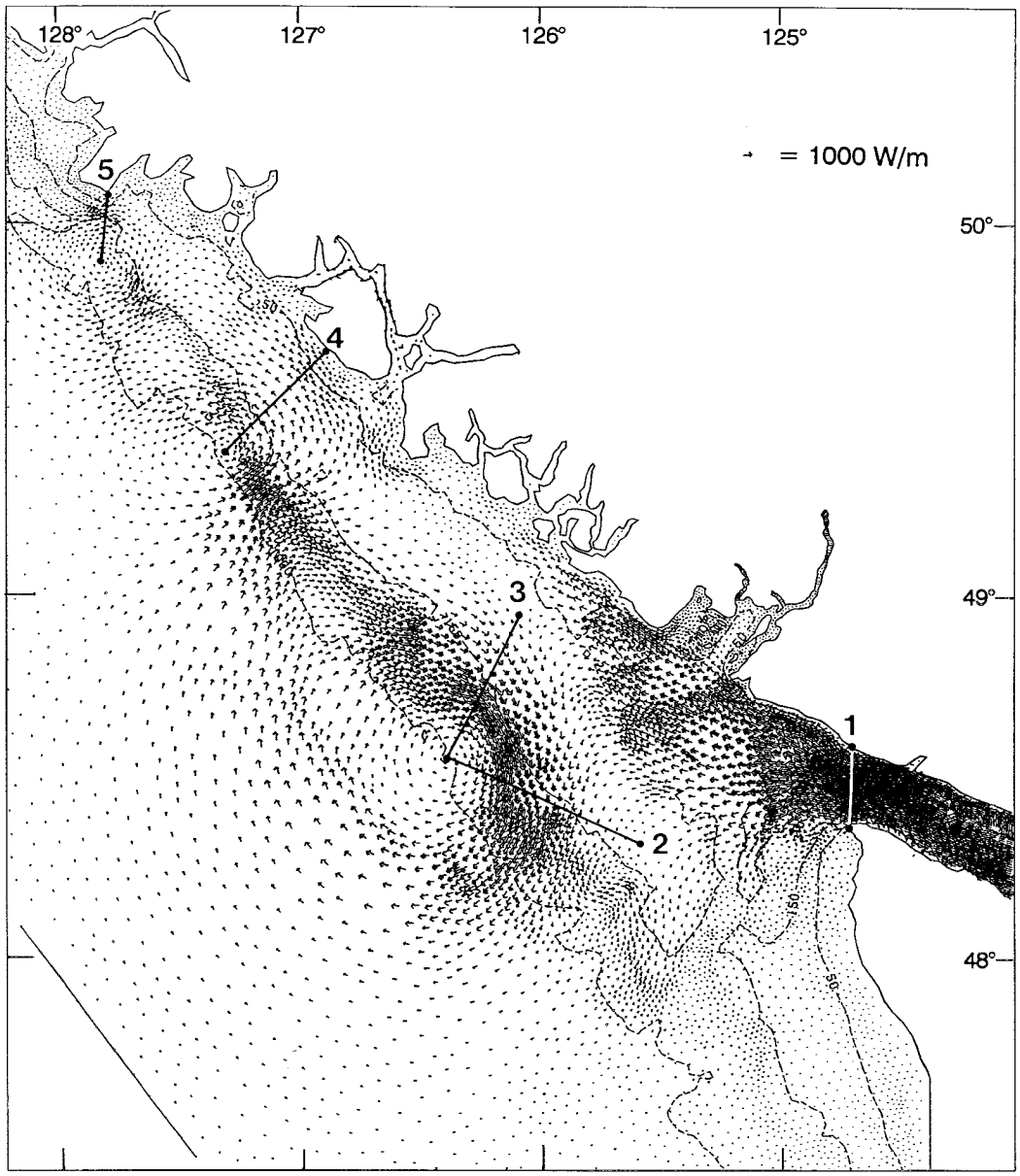

FIG. 10. Vertically integrated energy flux vectors for (a) K_1 and (b) O_1. Full shafts in a multishafted vector represent 1000 W m^{-1} and 250 W m^{-1}, respectively. Numbered transects are referenced in Tables 6 and 7 and are used for power calculations.

is much larger than the values shown in Tables 6 and 7. This is because the Kelvin wave component has a much larger surface elevation and much smaller velocities than its counterparts for the continental shelf wave. Consequently, the η contribution toward the total diurnal energy flux in Eq. (10) is dominated by the Kelvin wave component, while the $\bar{\mathbf{u}}$ contribution is dominated by the continental shelf waves. The net result [consistent with Crawford (1984) and F88] is that the combined K_1 energy flux vectors are approximately twenty times larger than those shown in Fig. 10a.

7. Resonance

The different energy flux patterns shown in Figs. 10a and 10b for constituents K_1 and O_1 suggest a resonant match/mismatch relationship between the wavelength of the continental shelf waves and the spacing of canyons along the shelf break. To investigate this further, a series of model runs were performed with a spectrum of frequencies forcing the velocities in Juan de Fuca Strait. The same velocity amplitudes and phases that were employed earlier for K_1 were used for these new runs and

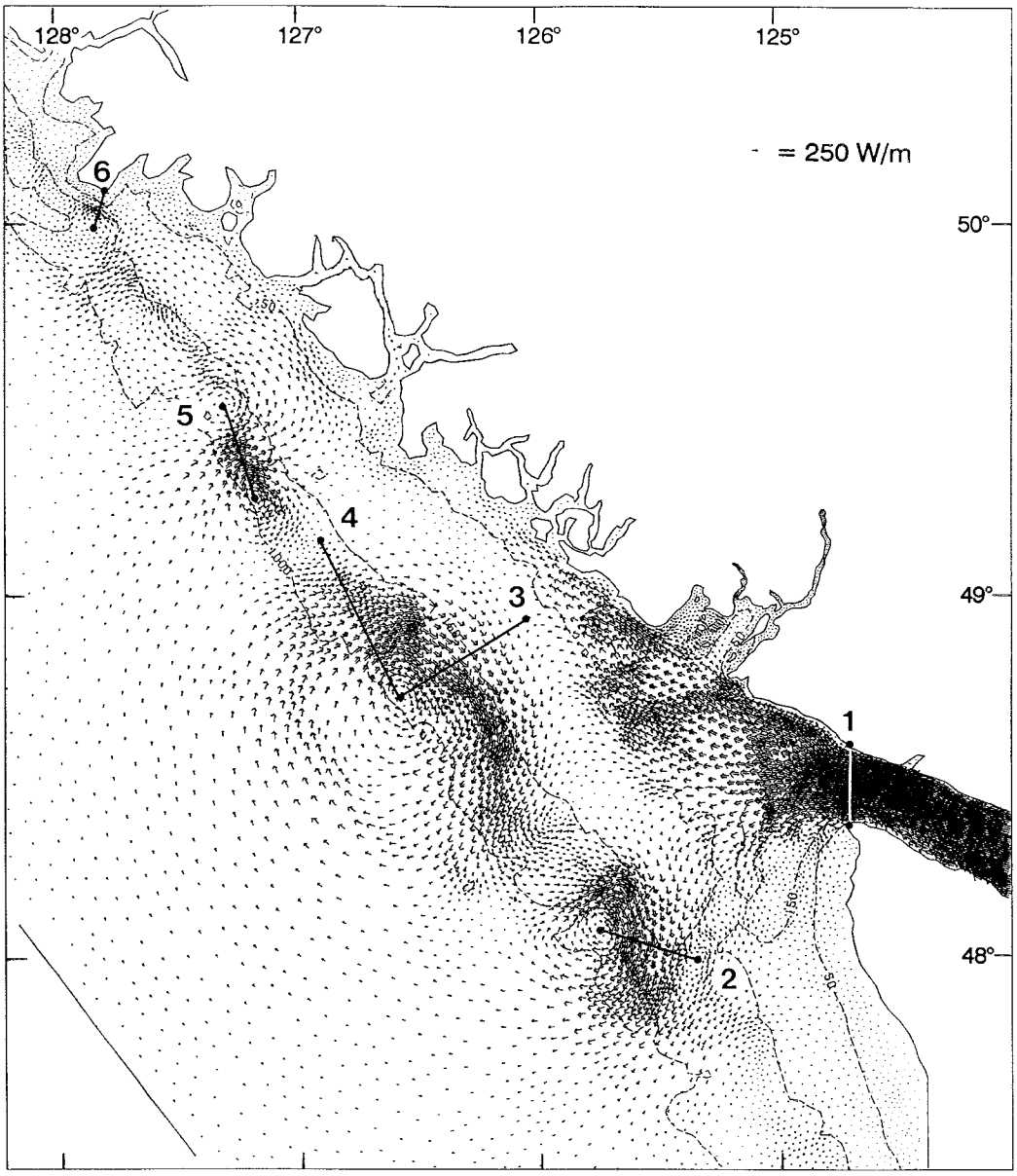

FIG. 10. (*Continued*)

the forcing frequency ranged between 0.002 and 0.070 cycles per hour. As the location of the energy eddies along the shelf break with K_1 and O_1 are largely determined by local highs and lows in the surface elevation amplitude, plots of this field were used as the standard for comparison. (The energy flux vectors cycle clockwise around local maxima in the η amplitudes and counterclockwise around local minima.)

With low-frequency forcing, the resultant η amplitude fields generally decreased from northeast to southwest in Juan de Fuca Strait and seaward from the Vancouver Island coast. There were minor irregularities corresponding to the bathymetry but the contours were generally smooth and there was no evidence of a wavelike pattern along the shelf break. However, a wave pattern began to emerge when $\omega/2\pi$ reached 0.016 cph and became most evident with $\omega/2\pi = 0.030$ cph. This response (as seen in Fig. 11a) shows six wavelengths along the shelf break between Washington State and Brooks Peninsula. Clearly, these wavelengths are quite variable and there appears to be some correlation with their position and those of canyons along the shelf break. [Further analysis, along the lines of Wilkin and Chapman (1990), is clearly required but beyond the scope of this paper.] As the forcing frequency became larger [passing through the O_1 and K_1 (Fig. 11b) values], there were fewer local extrema in the amplitude field. Finally as $\omega/2\pi$ approached the inertial frequency of 0.063 cph

TABLE 6. Integral of the normal component of the vertically integrated K_1 energy flux (megawatts) along the transects shown in Fig. 10a.

Name	Number	Power
Juan de Fuca	1	107.5
Eddy 1 to southeast	2	75.0
Eddy 1 to northeast	3	60.6
Eddy 2 to northeast	4	31.2
Eddy 3 to north	5	7.2

TABLE 7. Integral of the normal component of the vertically integrated O_1 energy flux (megawatts) along the transects shown in Fig. 10b.

Name	Number	Power
Juan de Fuca	1	29.8
Eddy 1 to southeast	2	11.2
Eddy 2 to northeast	3	15.2
Eddy 2 to northwest	4	15.8
Between eddies 3 and 4	5	9.7
Eddy 5 to north	6	0.4

(for lat 48.5°) the amplitudes simply decayed smoothly from their relatively large values in Juan de Fuca Strait; a pattern similar to that observed and simulated for the semidiurnal constituents.

A similar experiment was performed with forcing only in Queen Charlotte Strait. Although the current speeds were smaller than those generated with the Juan de Fuca Strait forcing (consistent with Fig. 7), the elevation amplitudes did show some indication of resonance along the shelf break. At low and near-inertial frequencies these amplitudes generally decreased smoothly away from the forcing region. With diurnal forcing a pair of local high and low values emerged along the shelf break and were most clearly defined with $\omega/2\pi = 0.036$ cph. However, the proximity of the northern boundary and the potential contaminating effects of the condition imposed there suggests that there can be little confidence in these results until the experiment is repeated with a larger domain.

8. Summary and discussion

The preceding presentation has detailed the verification of a three-dimensional model for simulating the barotropic tides and seasonal bouyancy flows off the western and northern coasts of Vancouver Island. Particular attention was given to the generation, seasonal variability, and energy budgets of the diurnal continental shelf waves.

Tidal elevations were seen to be represented quite accurately with the rms difference between model amplitudes and those calculated from observations being within 2.3 cm for all eight constituents included in the model simulations. Similar differences in the phases were, with the exception of constituent Q_1, all within 3.5°. However, the tidal model currents were generally less accurate due, in a large part, to the absence of baroclinic effects in the model physics. Baroclinic semidiurnal tides and baroclinic coastal-trapped waves are excluded by the model. Nevertheless, the model currents were an improvement over those from previous models and did shed further light on the generation and propagation of the diurnal shelf waves.

In particular, it was shown that the dominant clockwise rotary component of the shelf waves arises solely from the oscillatory flows in Juan de Fuca Strait. Energy flux plots for the K_1 and O_1 continental shelf waves revealed a series of localized eddies along the shelf break, south of Brooks Peninsula. An associated power budget analysis demonstrated that the sum of the power in these eddies is approximately equal to the power emanating from Juan de Fuca Strait. This balance indicates that although Brooks Peninsula and the extremely narrow continental shelf off its tip may act as barrier to low-frequency continental shelf waves, the peninsula is not a barrier to the diurnal waves propagating along western Vancouver Island because these waves have little energy left by the time they reach the peninsula. This conclusion was substantiated with a run where the model grid was modified by replacing the peninsula with a coastline and bathymetry that were smooth extensions of those to the northwest and southeast. Forcing in Juan de Fuca Strait produced virtually the same results as those runs with the grid that included Brooks Peninsula. Since the flux of energy must be conserved, the eddying regions must also be regions of enhanced frictional dissipation relative to other parts of the shelf. However, consistent with the analytical results of Wilmott and Thomson (1994), similar runs with forcing only in Queen Charlotte Strait did not produce the large diurnal currents observed around Goose Island, Cook, and Middle Banks. These currents must therefore arise from forcing through the oceanic boundaries.

Summer and winter buoyancy-driven currents were also calculated diagnostically and qualitatively compared to previously published subtidal observations. The interaction of these buoyancy flows with the continental shelf waves reproduced the observed seasonal phase shift at the current meter location off Estevan Point. The reason that the model produced a similar, but not observed, shift along the shelf break is not known. Future studies with baroclinic models should determine if our homogeneous density field is the cause of this discrepancy.

A simple experiment was also performed to better understand the shelf wave response to a spectrum of forcing in Juan de Fuca Strait. Though further analysis is clearly required, it appears that the number of eddies trapping energy along the shelf break is a function of both the forcing frequency and the spacing of canyons. A maximum of six wavelengths between the Washington State shelf and Brooks Peninsula were generated with periodic forcing of 0.030 cph.

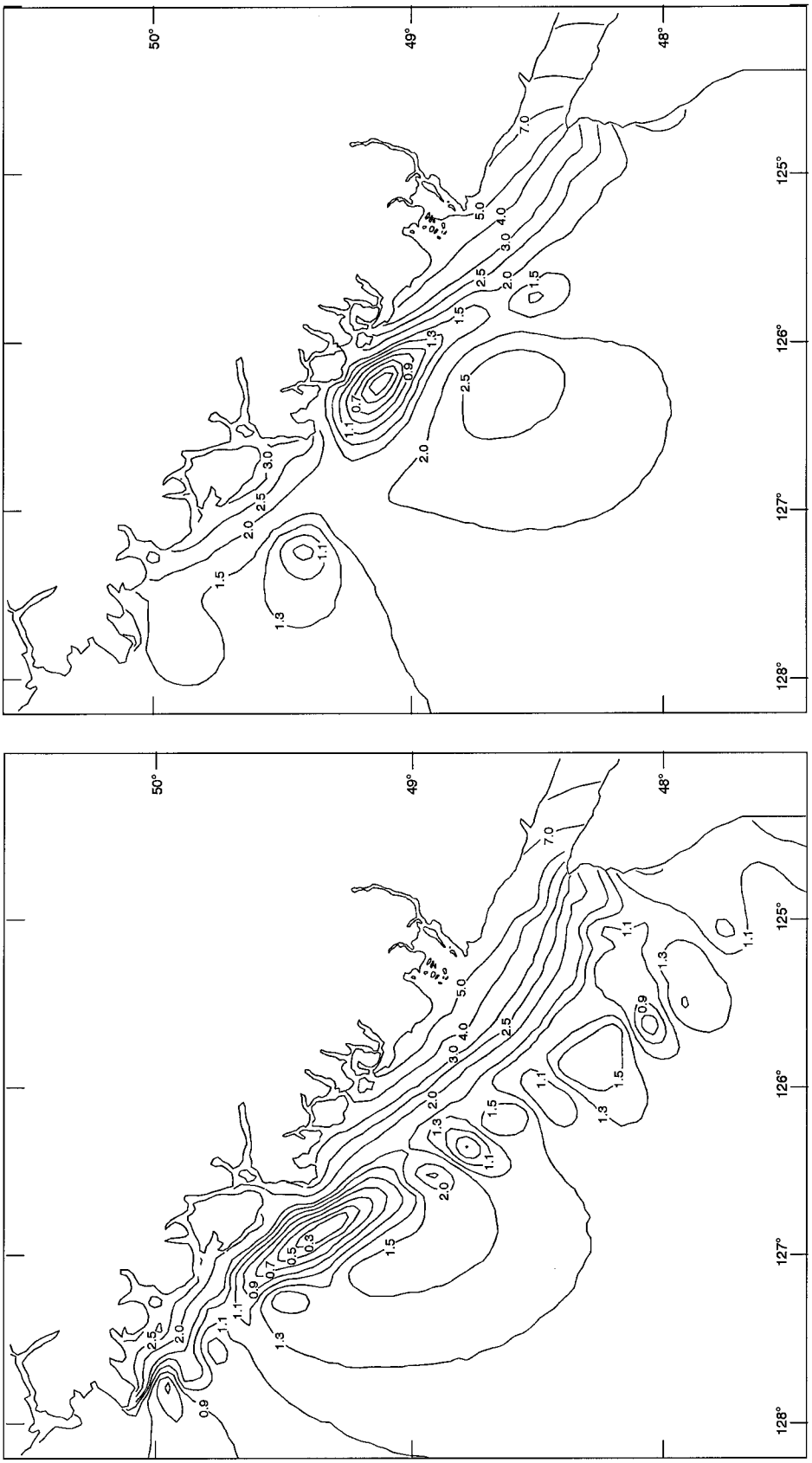

FIG. 11. Coamplitudes (cm) for Juan de Fuca Strait velocity forcing with (a) $\omega/2\pi = 0.030$ cph and (b) the K_1 frequency.

Acknowledgments. We thank Roy Walters for the use of his model code and helpful comments; Howard Freeland for the CODE-II current meter data; Bill Crawford, Patrick Cummins, Mike Woodward, Fred Stephenson, and Bodo de Lange Boom for helpful comments and/or observational data; Anne Ballantyne for analyzing many of the tide gauge and current meter time series; Patricia Kimber for drafting some of the figures; and the reviewers for their constructive criticism of an earlier version of the paper.

REFERENCES

Aldridge, J. N., and A. M. Davies, 1993: A high-resolution three-dimensional hydrodynamic tidal model of the eastern Irish Sea. *J. Phys. Oceanogr.,* **23,** 207–224.

Ballantyne, V. A., M. G. G. Foreman, W. R. Crawford, and R. Jacques, 1996: Three-dimensional model simulations for the north coast of British Columbia. *Contin. Shelf Res.,* **16**(13), 1655–1682.

Brink, K. H., 1982: A comparison of long coastal trapped wave theory with observations off Peru. *J. Phys. Oceanogr.,* **12,** 897–913.

Crawford, W. R., 1984: Energy flux generation of diurnal shelf waves along Vancouver Island. *J. Phys. Oceanogr.,* **14,** 1599–1607.

——, and R. E. Thomson, 1984: Diurnal period shelf waves along Vancouver Island: A comparison of observations with theoretical models. *J. Phys. Oceanogr.,* **14,** 1629–1646.

Cummins, P., and L.-Y. Oey, 1997: Simulation of barotropic and baroclinic tides off northern British Columbia. *J. Phys. Oceanogr.,* **27,** 762–781.

Davies, A. M., 1990: On extracting tidal current profiles from vertically integrated two-dimensional hydrodynamic models. *J. Geophys. Res.,* **95**(C10), 18 317–18 342.

——, 1993: Numerical problems in simulating tidal flows with a friction velocity dependent eddy viscosity and the influence of stratification. *Int. J. Numer. Methods Fluids,* **16,** 105–131.

Denman, K. L., and H. J. Freeland, 1985: Correlation scales, objective mapping and a statistical test of geostrophy over the continental shelf. *J. Mar. Res.,* **43,** 517–539.

Drakopoulos, P., and R. F. Marsden, 1993: The internal tide off the west coast of Vancouver Island. *J. Phys. Oceanogr.,* **23,** 758–775.

Egbert, G. D., A. F. Bennett, and M. G. G. Foreman, 1994: TOPEX/POSEIDON tides estimated using a global inverse model. *J. Geophys. Res.,* **99**(C12), 24 821–24 852.

Flather, R. A., 1987: A tidal model of the northeast Pacific. *Atmos.–Ocean,* **25**(1), 22–45.

——, 1988: A numerical model investigation of tides and diurnal-period continental shelf waves along Vancouver Island. *J. Phys. Oceanogr.,* **18,** 115–139.

Foreman, M. G. G., 1978: Manual for tidal currents analysis and prediction. Pacific Marine Sci. Rep. 78-6, 70 pp. [Available from Dept. of Fisheries and Oceans, Institute of Ocean Sciences, P.O. Box 6000, Sidney BC V8L 4B2, Canada.]

——, and R. A. Walters, 1990: A finite-element tidal model for the southwest coast of Vancouver Island. *Atmos.–Ocean,* **28,** 261–287.

——, R. E. Thomson, D. R. Lynch, and R. A. Walters, 1992: A finite element model for three-dimensional flows along the west coast of Vancouver Island. *Estuarine and Coastal Modeling,* Second Int. Conf./WW Div. ASCE, Tampa, FL, 574–585.

——, R. F. Henry, R. A. Walters, and V. A. Ballantyne, 1993: A finite element model for tides and resonance along the north coast of British Columbia. *J. Geophys. Res.,* **98**(C2), 2509–2531.

——, R. A. Walters, R. F. Henry, C. P. Keller, and A. G. Dolling, 1995: A tidal model for eastern Juan de Fuca Strait and the southern Strait of Georgia. *J. Geophys. Res.,* **100**(C1), 721–740.

Fortunato, A. B., and A. M. Baptista, 1996: Evaluation of horizontal gradients in sigma-coordinate shallow water models. *Atmos.–Ocean,* **34**(3), 489–514.

Freeland, H. J., 1988: Derived Lagrangian statistics on the Vancouver Island continental shelf and implications for salmon migration. *Atmos.–Ocean,* **26**(2), 267–281.

——, W. R. Crawford, and R. E. Thomson, 1984: Currents along the Pacific coast of Canada. *Atmos.–Ocean,* **22,** 151–172.

Gill, A. E., 1982: *Atmosphere–Ocean Dynamics.* Academic Press, 662 pp.

Gross, T. F., and F. E. Werner, 1994: Residual circulations due to bottom roughness variability under tidal flows. *J. Phys. Oceanogr.,* **24,** 1494–1502.

Haney, R. L., 1991: On the pressure gradient force over steep topography in sigma coordinate ocean models. *J. Phys. Oceanogr.,* **21,** 610–619.

Hannah, C. G., and D. G. Wright, 1995: Depth dependent analytical and numerical solutions for wind-driven flow in the coastal ocean. *Quantitative Skill Assessment for Coastal Ocean Models,* D. R. Lynch and A. M. Davies, Eds., Coastal and Estuarine Studies, Vol. 47, Amer. Geophys. Union, 125–152.

Heaps, N. S., J. M. Huthnance, J. E. Jones, and J. Wolf, 1988: Modelling of storm-driven shelf waves north of Scotland—I. Idealized models. *Contin. Shelf Res.,* **8,** 1187–1210.

Henry, R. F., and M. G. G. Foreman, 1977: Numerical model studies of semi-diurnal tides in the southern Beaufort Sea. Pacific Mar. Sci. Rep. 77-11, 71 pp. [Available from Dept. of Fisheries and Oceans, Institute of Ocean Sciences, P.O. Box 6000, Sidney, BC V8L 4B2, Canada.]

——, and R. A. Walters, 1993: A geometrically-based, automatic generator for irregular triangular networks. *Commun. Numer. Methods Eng.,* **9,** 555–566.

Hickey, B. M., R. E. Thomson, H. Yih, and P. H. LeBlond, 1991: Velocity and temperature fluctuations in a buoyancy-driven current off Vancouver Island. *J. Geophys. Res.,* **96**(C6), 10 507–10 538.

Hsieh, W. W., 1982: On the detection of continental shelf waves. *J. Phys. Oceanogr.,* **12,** 414–427.

Kang, S. K., J.-Y. Chung, S.-R. Lee, and K.-D. Yum, 1995: Seasonal variability in the M_2 tide in the seas adjacent to Korea. *Contin. Shelf Res.,* **15**(9), 1087–1113.

Kowalik, Z., and A. Y. Proshutinsky, 1993: Diurnal tides in the Arctic Ocean. *J. Geophys. Res.,* **98**(C9), 16 449–16 468.

Loder, J. W., and D. G. Wright, 1985: Tidal rectification and frontal circulation on the sides of Georges Bank *J. Mar. Res.,* **43,** 582–604.

Luettich, R. A., and J. J. Westerink, 1995: Continental shelf scale convergence studies with a barotropic tidal model. *Quantitative Skill Assessment for Coastal Ocean Models,* D. R. Lynch and A. M. Davies, Eds., Coastal and Estuarine Studies; Vol. 47, Amer. Geophys. Union, 349–372.

Lynch, D. R., and C. E. Naimie, 1993: The M_2 tide and its residual on the New England Banks of the Gulf of Maine. *J. Phys. Oceanogr.,* **23,** 2222–2253.

——, F. E. Werner, D. A. Greenberg, and J. W. Loder, 1992: Diagnostic model for baroclinic, wind-driven and tidal circulation in shallow seas. *Contin. Shelf Res.,* **12,** 37–64.

McDonnell, P. W., 1979: *Introduction to Map Projections.* Marcel Dekker, 174 pp.

Munk, W. H., and E. R. Anderson, 1948: Notes on a theory of the thermocline. *J. Mar. Res.,* **7,** 276–295.

Naimie, C. E., J. W. Loder, and D. R. Lynch, 1994: Seasonal variation of the three-dimensional residual circulation on Georges Bank. *J. Geophys. Res.,* **99**(C8), 15 967–15 989.

Rabinovich, A. B., and Y. E. Zhukov, 1984: Tidal oscillations on the shelf of Sakhalin Island. *Oceanology,* **24**(2), 184–189.

Snyder, R. L., M. Sidjabat, and J. H. Filloux, 1979: A study of tides, setup, and bottom friction in a shallow semi-enclosed basin. Part II: Tidal model and comparison with data. *J. Phys. Oceanogr.,* **9,** 170–188.

Soulsby, R. L., 1990: Tidal current boundary layers. *The Sea*, Vol. 9A, *Ocean Engineering Science.* John Wiley and Sons.

Thomson, R. E., 1981: Oceanography of the British Columbia coast. Canadian Special Publication Fisheries and Aquatic Sciences 56, 291 pp. [Available from Canadian Government Publishing Centre, Supply and Service Canada, Ottawa K1A OS9, Canada.]

——, and D. M. Ware, 1996: A current velocity index of ocean variability. *J. Geophys. Res.*, **101,** 14 297–14 310.

——, B. M. Hickey, and P. H. LeBlond, 1989: The Vancouver Island coastal current: Fisheries barrier and conduit. *Effects of Ocean Variability on Recruitment and an Evaluation of Parameters Used in Stock Assessment Models.* Vancouver, Canada, International Recruitment Investigations in the Subarctic, 265–296.

Vichnevetsky, R., 1987: Wave propagation and reflection in irregular grids for hyperbolic equations. *Appl. Numer. Math.*, **3,** 133–166.

Walters, R. A., 1992: A three-dimensional, finite element model for coastal and estuarine circulation. *Contin. Shelf Res.*, **12,** 83–102.

——, 1996: A model study of the effects of sea level rise in Delaware Bay and River. Part 1: Hydrodynamics. *J. Geophys. Res.*, in press.

Ware, D. M., and R. E. Thomson, 1993: La Pérouse Project, Eighth Annual Progress Rep. [Available from Department of Fisheries and Oceans, Institute of Ocean Sciences, P.O. Box 6000, Sidney, BC V8L 4B2, Canada.]

Werner, F. E., F. H. Page, D. R. Lynch, R. G. Lough, R. I. Perry, D. A. Greenberg, and M. M. Sinclair, 1993: Influences of mean advective and simple behaviour on the distribution of cod and haddock early life stages on Georges Bank. *Fish. Oceanogr.*, **2**(2), 43–64.

Wilkin, J. L., and D. C. Chapman, 1990: Scattering of coastal-trapped waves by irregularities in coastline and topography. *J. Phys. Oceanogr.*, **20,** 396–421.

Willmott, A. J., and R. E. Thomson, 1994: Forced shelf wave dynamics for a discontinuous shelf width: Application to Vancouver Island. *J. Phys. Oceanogr.*, **24,** 1347–1367.

Xing, J., and A. M. Davies, 1996: Application of turbulence energy models to the computation of tidal currents and mixing intensities in shelf edge regions. *J. Phys. Oceanogr.*, **26,** 417–447.